

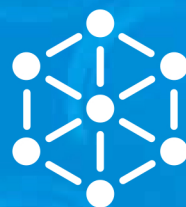
ISSN 1883 - 0315



TOHOKU  
UNIVERSITY

# IMR KINKEN Research Highlights 2018

Institute for Materials Research, Tohoku University



Research

# KINKEN

## Research Highlights

### 2018



Institute for Materials Research, Tohoku University

# KINKEN Research Highlights 2018

## Contents

<b>Preface</b> .....	4
----------------------	---

### Research Highlights

#### 1. Infrastructural Materials

Crystal Physics Division .....	8
Microstructure Design of Structural Metallic Materials Division.....	9
Materials Design by Computer Simulation Division.....	10
Environmentally Robust Materials Division .....	11
Chemical Physics of Non-Crystalline Materials Division .....	12
Deformation Processing Division .....	13
Analytical Science Division .....	14
Creation of Life Innovation Materials for Interdisciplinary and International Researcher Development.....	15

#### 2. Energy-Related Materials

Physics of Crystal Defects Division .....	18
Irradiation Effects in Nuclear and Their Related Materials Division.....	19
Physics of Electronic Materials Division .....	20
Structure-Controlled Functional Materials Division.....	21
Non-Equilibrium Materials Division.....	22
Hydrogen Functional Materials Division .....	23
Advanced Crystal Engineering Laboratory .....	24
Multi-Functional Materials Science Division .....	25

### 3. Electronic Materials

Theory of Solid State Physics Division .....	28
Magnetism Division .....	29
Surface and Interface Research Division .....	30
Low Temperature Physics Division .....	31
Low Temperature Condensed State Physics Division .....	32
Quantum Beam Materials Physics Division .....	33
Solid-State Metal-Complex Chemistry Division .....	34
Magnetic Materials Division .....	35
Crystal Chemistry Division .....	36
Actinide Materials Science Division .....	37
Materials Science of Non-Stoichiometric Compounds Division .....	38
Professional development Consortium for Computational Materials Scientists (PCoMS) .....	39

### Research Centers

International Research Center for Nuclear Materials Science .....	42
Cooperative Research and Development Center for Advanced Materials .....	44
High Field Laboratory for Superconducting Materials .....	45
Trans-Regional Corporation Center for Industrial Materials Research .....	46
Center for Computational Materials Science .....	47
Collaborative Research Center on Energy Materials .....	48
International Collaboration Center (ICC-IMR) .....	49
Center of Neutron Science for Advanced Materials .....	50
Laboratory of Low Temperature Materials Science .....	51
Laboratory of Alpha-Ray Emitters .....	52
Analytical Research Core for Advanced Materials .....	53

<b>Author Index</b> .....	54
---------------------------	----

<b>Keyword Index</b> .....	55
----------------------------	----



# Preface

Dear Colleagues,

We are pleased to present *KINKEN* Research Highlights 2018, which is the annual report that includes a collection of research outputs of the past year from the Institute for Materials Research (IMR), Tohoku University. *KINKEN* is the abbreviation for “Kinzoku Zairyo Kenkyujo,” the Japanese name for IMR, which is well known in the materials science community.

IMR celebrated its centenary in 2016. Professor Kotaro Honda established the IMR at the Tohoku Imperial University in 1916 as the 2<sup>nd</sup> Division of the Provisional Institute of Physical and Chemical Research. At that time the primary research focus was steel. Thereafter, the research domains gradually broadened to include various types of alloys and metals. The name was changed into the Research Institute for Iron, Steel and Other Metals (RIISOM) in 1922. Subsequently, the institute developed into a global center for fundamental and applied research covering all types of materials, including nonmetals. In 1987 the institute was reorganized into a national collaborative research institute affiliated with Tohoku University, and consequently renamed to the present Institute for Materials Research (IMR).

IMR has greatly contributed to the advancement of materials science and engineering. The invention of KS steel in 1916, the strongest permanent magnet at that time, was the first great achievement. In subsequent years, many different types of practically useable materials have successfully been developed, including new KS steel, Sendust alloy, SiC fibers, various intermetallic compounds, and more recently, amorphous alloys. In addition, considerable effort was dedicated to basic research for materials development, which paved the way for pioneering research in magnetism, superconductivity,



---

Director Prof. Koki Takanashi



optical properties, and microstructure analyses of materials. Recently, IMR has created a wide array of new materials, including high-performance, high-quality, and multifunctional materials such as bulk metallic glasses, nanostructured materials, nanocomposites, ceramics, crystals, oxides, nitrides, hydrides, complexes, organic materials, etc., which are useful for electronic, optical, magnetic, spintronic, biological, energetic, and infrastructural applications.

In the 21st Century, we face worldwide environmental problems such as global warming and the depletion of resources and energy. There is an increasing need to preserve the environment and work towards achieving sustainable societies. IMR upholds these themes with the objective of “contributing to the well being of the human race and the development of civilization through the creation of new materials that are truly useful to society”.

We hope that the KINKEN Research Highlights will enable you to better understand our recent research activities and will aid the promotion of worldwide collaboration with IMR. We ask for your continued support and welcome any suggestions.

# *Infrastructural Materials*

IMR KINKEN Research Highlights 2018



## Subgrain Boundary Energy of Copper at Melting Temperature

Grain boundary energy influences the morphology of the crystal/melt interface of polycrystalline materials during solidification. However, it is quite hard to experimentally measure the grain boundary energy of metals at their melting temperature. We overcame the experimental difficulties and determined the grain boundary energy of copper by an in-situ observation method.

The shape of the grain boundary groove is determined by the force balance between the crystal/melt interface energy ( $\sigma_{sl}$ ) and the grain boundary energy ( $\sigma_{gb}$ ). Therefore, if we could observe the grain boundary groove at an equilibrated crystal/melt interface, we could measure  $\sigma_{gb}$  at the melting temperature. In this study, we attempted to directly observe the grain boundary groove at the crystal/melt interface in pure copper (Cu).

The experiment was conducted with an *in-situ* observation system consisting of a furnace and a digital optical microscope.

Figure 1 shows the morphological change in the grain boundary groove during the directional solidification of pure Cu [1]. Clearly, the groove gradually deepened, and its shape changed. This indicated that we had to maintain the interface under equilibrium conditions to be able to measure  $\sigma_{gb}$  from the groove shape. Thus, we attempted to keep the interface in equilibrium. If, for an extended period of time, the crystal/melt interface does not move, melt, or grow, the interface can be assumed to be at the melting temperature.

Thus, we adjusted the temperature precisely by monitoring the crystal/melt interface. Figure 2 shows the stationary crystal/melt interface [1]. To determine the shape of the groove, the contrast and brightness of each image was changed prior to the analysis.

It was shown that the position of the planar interface did not change, which indicated that the temperature at the crystal/melt interface was maintained at the melting temperature of Cu (1358 K). The shape of the grain boundary groove is determined by the force balance indicated in Fig. 2, which can be expressed as  $\sigma_{gb} = (\cos\theta_1 + \cos\theta_2) \sigma_{sl}$ .

The crystal/melt interfacial energy of Cu at its melting temperature was reported to be  $\sigma_{sl} = 0.2724$  ( $\text{J m}^{-2}$ ), and  $\theta_1$  and  $\theta_2$  could be measured from the images in Fig. 2. Thus, we could estimate  $\sigma_{gb}$ . The observed grain boundary was found to be a subgrain boundary by electron backscattering pattern analysis. The values of the  $\sigma_{gb}$  estimates are listed in Fig. 2. The estimates of  $\sigma_{gb}$  (subgrain boundary) ranged between 0.234 and 0.296  $\text{J m}^{-2}$ .

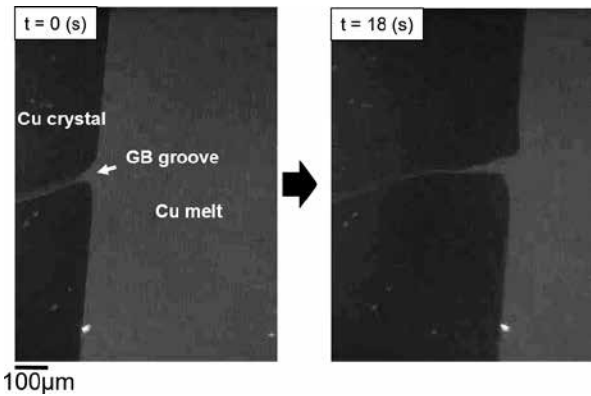


Fig. 1 Grain boundary groove during the directional solidification of pure Cu.

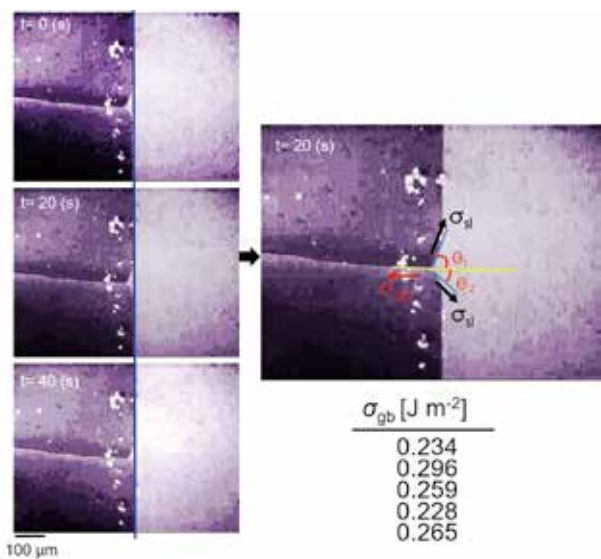


Fig. 2 (left) Equilibrated crystal/melt interface. (right) Measurement of grain boundary energy.

In this way, the equilibrated crystal/melt interface with a grain boundary groove was established by controlling the temperature through monitoring the sample state, which enabled the measurement of the grain boundary energy,  $\sigma_{gb}$ .

### References

- [1] K. Maeda, A. Niitsu, H. Morito, K. Shiga, and K. Fujiwara, *Scr. Mater.* **146**, 169 (2018).

Keywords: crystal growth, interface  
 Kozo Fujiwara (Crystal Physics Division)  
 E-mail: kozo@imr.tohoku.ac.jp  
 URL: <http://www.xtalphys.imr.tohoku.ac.jp/>

## Influence of Driving Force for Precipitation on Dispersion of Vanadium Carbide Interphase Precipitation in Low-Carbon Steels

As a controlling factor on the dispersion of nanosized interphase precipitation formed at the migrating ferrite/austenite interface during ferrite transformation, the driving force for its precipitation is estimated in this study by quantitatively measuring the interfacial composition in vanadium-microalloyed low-carbon steels. Following our expectation, the estimated driving force shows good correlation with both the number density and average radius of vanadium carbide.

The interphase precipitation of nanosized alloy carbide occurs at the migrating ferrite/austenite interface during ferrite transformation in steels containing strong carbide-forming elements, *e.g.*, vanadium, niobium, or titanium. Compared with normal precipitation by aging from a supersaturated matrix, interphase precipitation features rapid precipitation kinetics, facilitated by both local enrichment in the solute and higher diffusivity at the interphase boundary.

In this study, we try to correlate the driving force for interphase precipitation with the resultant dispersion of nanosized alloy carbide in vanadium-microalloyed low-carbon steels. The driving force was quantitatively estimated based on the interfacial composition measured by using electron probe microanalysis. In order to eliminate the influence of interfacial coherency [1], only ferrite grains without a specific highly coherent orientation relationship were purposely selected to quantify the dispersion of vanadium carbide interphase precipitation by atomic probe tomography.

Figure 1 shows a vanadium atom map of ferrite with nanosized vanadium carbide as a typical example of interphase precipitation. Figure 2 shows the variations in number density and average radius of vanadium carbide with estimated driving force, respectively, which is formed under various conditions, *e.g.*, at different transformation temperatures or with different bulk alloy compositions. The overall tendency can be summarized as: interphase precipitation increases in number density and decreases in size with larger driving force, which is reasonable from the viewpoint of facilitated nucleation [2]. Based on this result, the strategy for further strengthening the interphase precipitation-strengthened automobile steels should be refinement in particle dispersion by increasing the driving force through better alloy design and processing.

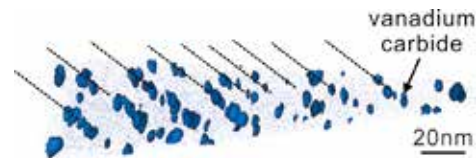


Fig. 1 Typical vanadium atom map of ferrite with vanadium carbide interphase precipitation.

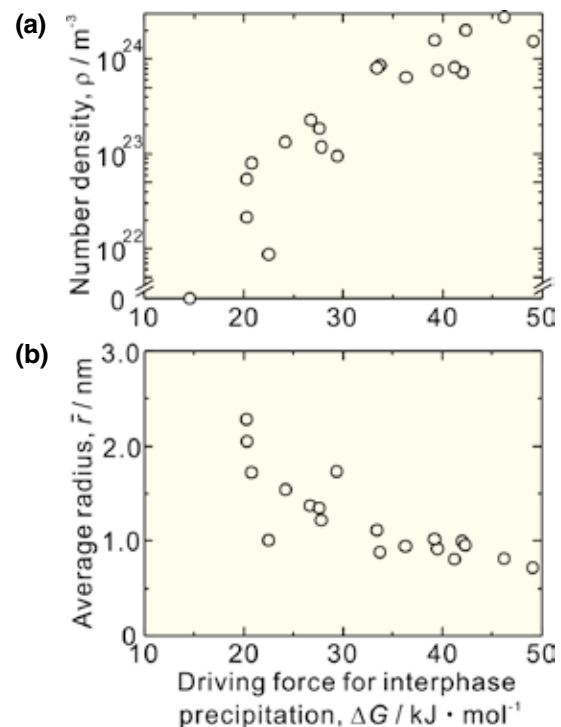


Fig. 2 Relationship between (a) number density and (b) average radius of vanadium carbide with driving force for interphase precipitation formed under various conditions.

### References

- [1] Y.-J. Zhang, G. Miyamoto, K. Shinbo, and T. Furuhashi, *Scr. Mater.* **69**, 17 (2013).
- [2] Y.-J. Zhang, G. Miyamoto, K. Shinbo, and T. Furuhashi, *Acta Mater.* **128**, 166 (2017).

Keywords: phase transformation, interface, steel

Yongjie Zhang (Microstructure Design of Structural Metallic Materials Division)

E-mail: yongjie@imr.tohoku.ac.jp

URL: <http://www.st-mat.imr.tohoku.ac.jp>

## Superlarge-Scale Molecular Dynamics Simulation for Fracture of Materials

The novel development of high-performance and long-life materials needs a deep understanding of the fracture processes of materials. These processes consist of multiphysics and multiscale phenomena including chemical reactions on the nanoscale and physical phenomena such as friction, impact, stress, and fluid on the macroscale. We are pioneering advanced materials design based on superlarge-scale simulation for the elucidation of multiphysics and multiscale phenomena.

To realize a safe and secure society, the novel development of high-performance and long-life materials is necessary. These material technologies require a deep understanding of fracture processes, which consist of multiphysics and multiscale phenomena including chemical reactions on the nanoscale and physical phenomena such as friction, stress, and fluid on the macroscale. Thus, we have investigated multiphysics and multiscale phenomena by computational simulation methods. [1-3] Here, superlarge-scale simulations can precisely elucidate the multiphysics and multiscale phenomena in the fracture process. Then, we applied our superlarge-scale molecular dynamics code for pioneering next-generation materials design.

In order to reveal fracture processes of the lamellar structure in polyethylene, we performed coarse-grained superlarge-scale molecular dynamics simulations, which can be directly compared with electron microscopy images. Here, we constructed a large-scale lamellar structure consisting of three million monomers (Fig. 1). While stretching parallel to the crystal direction, the structural change from amorphous to crystalline layers increases the compression and the generation of voids in the amorphous layers. We found that the change in the polymer lamella structure lowers the stress in the polymer materials [1].

Ni sintering in the Ni/YSZ porous anode of a solid oxide fuel cell changes the porous structure, leading to degradation. To prevent the sintering and degradation, we need to elucidate the effects of the particle size on sintering. In this study, we developed a superlarge-scale molecular dynamics simulator with a multimillion-atom Ni/YSZ multi-nanoparticle model and investigated the effects of YSZ particle size on the sintering and degradation in the Ni/YSZ anodes. At first, we compared the sintering processes in the Ni/YSZ models with YSZ particle diameters of 6 and 2 nm. When the diameter is 6

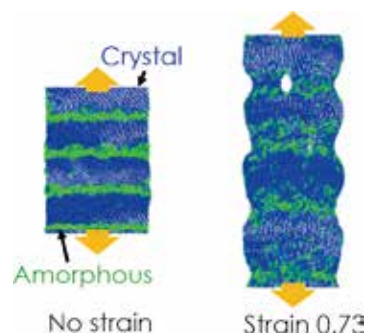


Fig. 1 Fracture simulation of polymer lamella structure with three million monomers.

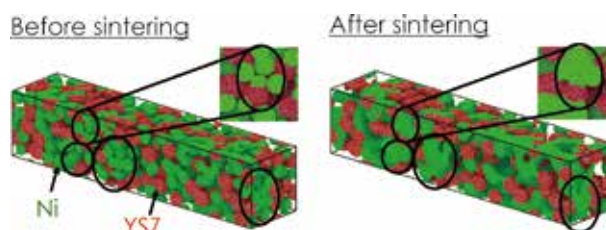


Fig. 2 Snapshots of Ni sintering simulations of the multimillion-atom Ni/YSZ multi-nanoparticle model with YSZ particle diameter of 6 nm.

nm, some Ni nanoparticles form a large compact aggregate owing to sintering (Fig. 2). Moreover, the pores in the Ni/YSZ multi-nanoparticle model coalesce because of the sintering and the diffusion path of hydrogen gas is blocked. In contrast, when the diameter is 2 nm, pore coalescence is not observed. Thus, we found that the gas diffusion performance degrades as the YSZ particle size increases [2].

### References

- [1] Y. Higuchi and M. Kubo, *Macromolecules*. **50**, 3690 (2017).
- [2] J. Xu, Y. Higuchi, N. Ozawa, K. Sato, T. Hashida, and M. Kubo, *ACS Appl. Mater. Interfaces*. **9**, 31816 (2017).
- [3] Y. Wang, J. Xu, Y. Ootani, S. Bai, Y. Higuchi, N. Ozawa, K. Adachi, J.M. Martin, and M. Kubo, *ACS Appl. Mater. Interfaces*. **9**, 34396 (2017).

Keywords: simulation, molecular dynamics, fracture  
 Momoji Kubo (Materials Design by Computer Simulation Division)  
 E-mail: momoji@imr.tohoku.ac.jp  
 URL: <http://www.simulation.imr.tohoku.ac.jp/>

## Hydrogen Uptake Under Conventional Electrochemical Hydrogen Charging

Hydrogen uptake behaviors under galvanostatic and potentiostatic hydrogen charging conventionally used for hydrogen embrittlement studies have been examined by using an electrochemical hydrogen permeation technique. A guideline for efficient hydrogen charging covering a wide range of hydrogen content by changing the catalyst poison concentration and current density or potential has been obtained.

Electrochemical hydrogen charging is commonly utilized in order to charge specimens of high-strength steels and other metals with hydrogen for the examination of their hydrogen embrittlement properties, owing to its ease and low cost. Furthermore, cathodic hydrogen charging has a high fugacity of hydrogen compared to that in high-pressure hydrogen gas at high temperature. However, the details of the procedures of hydrogen charging are barely reported, and the hydrogen content in specimens is often controlled in a trial-and-error manner.

To understand the hydrogen uptake behavior under electrochemical hydrogen charging conditions, we adopted an electrochemical hydrogen permeation technique using pure Fe sheet specimens in some conventionally used aqueous solutions with varied concentrations of  $\text{NH}_4\text{SCN}$ , which enhances hydrogen entry.

Figure 1 shows that various hydrogen permeation current densities can be obtained by controlling the hydrogen charging current density [1] or potential [2], and  $\text{NH}_4\text{SCN}$  concentration.

Essentially, the hydrogen permeation current density varies with the logarithm of the current density and similarly with potential, because the logarithm of the current density and potential on the hydrogen input side are linearly related, suggesting a potential-dependent surface coverage of adsorbed hydrogen.

Because the hydrogen permeation current density is considered to be proportional to the diffusible hydrogen content, the resulting hydrogen content for any given hydrogen charging condition can be estimated if the hydrogen content obtained in one condition is measured by means of thermal desorption analysis. Therefore, the relationships can be used as a guideline for hydrogen charging.

However, the hydrogen permeation current density tended to increase with time in a  $\text{NH}_4\text{SCN}$ -containing solution during both galvanostatic and potentiostatic hydrogen charging, suggesting that it

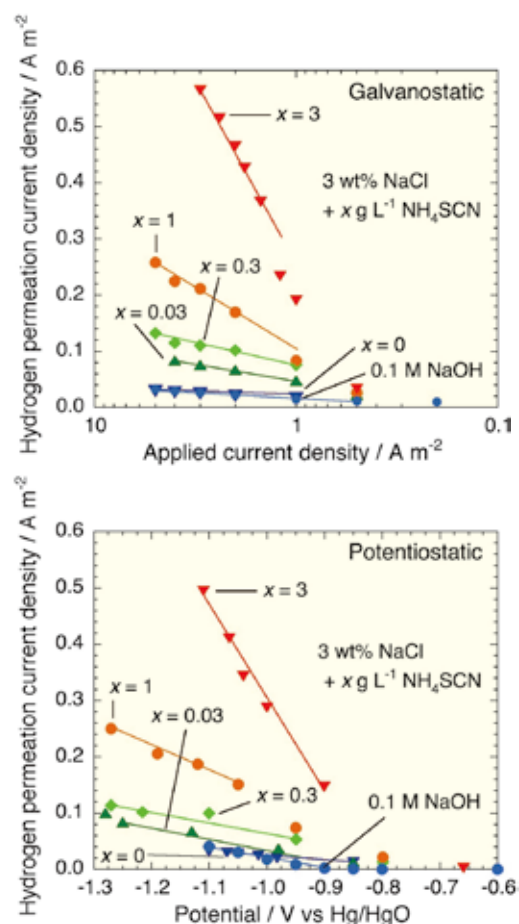


Fig. 1 Relationship between hydrogen permeation current density and logarithm of applied current density (top) and applied potential (bottom) of hydrogen input side for galvanostatic and potentiostatic hydrogen charging, in various aqueous solutions with/without  $\text{NH}_4\text{SCN}$ .

is recommended to measure the resulting hydrogen content by means of thermal desorption analysis for accuracy, although the obtained relationship can be used as an approximate standard.

### References

- [1] E. Akiyama and S. Li, *Corros. Rev.* **34**, 103 (2016).
- [2] E. Akiyama and S. Li, *ECS Trans.* **75**, 22 (2017).

Keywords: corrosion, high-strength steel, surface reaction  
Eiji Akiyama (Environmentally Robust Materials Division)  
E-mail: akiyama@imr.tohoku.ac.jp  
URL: <https://akiyamaimr.amebaownd.com/>

## Crystal Structure of C-AlRuNi with Pseudo-Mackay Cluster

The structure of C-AlRuNi (1/0 approximant) is composed by the alternative linkage of the type-A pseudo-Mackay cluster (pMC-A) and the mini-Bergman cluster (mini-BC) with a regular Al-icosahedron (Al-IC). The chemical variation of a series of 1/0 approximants is also discussed by using the unique shell structure of pMCs.

Mackay clusters and mini-Bergman clusters (mini-BCs) are common building units for the icosahedral phase and their distribution provides an interesting overview of the structures of crystalline approximants. As an example, recent analyses of R-AlPdCo and F-AlPdCoGe [1-2] demonstrated the unique linkage of pseudo-Mackay clusters (pMCs) and mini-BCs connected by sharing the edges of their inner heavy metal icosahedra (HM-ICO). Knowledge of the approximant structures also allows us to suggest the importance of an Al icosahedron with a TM center (Al-ICO) as a glue unit in the connection of pMCs.

In the phase diagrams of Al-(Cu, Ni, or Pd)-(Co, Ru, Rh, Fe, or Ir), three types of 1/0 cubic approximants (C, C1, and C2) were recognized in the composition range of 60–80mol% Al. The C phase is located in the relatively Al-rich and HM-poor region compared to that for the C2 phase, and the C1 phase is realized in the middle region. This finding strongly suggests a significant relationship between the crystal structures and the chemical compositions of these approximants.

The structure of C-AlNiRu [3] is composed of a 3-D framework consisting of the regular heavy metal icosahedron (H-rICO) and a rather irregular shaped one (H-ilICO), as shown in Fig. 1. H-rICO has the inner shell of an Al-cube with a heavy metal center and the outer shell of an Al-icosi-dodecahedron, indicating an atomic arrangement similar to pMC. However, H-ilICO has an inner shell of an Al-ICO and could be ranked by mini-BC. In other words, pMC is located at the origin of the unit cell and the glue unit of an Al-ICO with a Ni center is located at the center of the unit cell.

It is interesting to note the chemical composition for the 1/0 approximants by using the structural variation of pMCs. The atomic arrangement of the inner shell of pMCs could be classified into three types (hereafter pMC-A, pMC-B, and pMC-C) [1-2]. The pMC-A type has an Al-polyhedron with a HM center, pMC-B shows a harmony of an Al-cube and an octahedron of HM and Al, and pMC-C has a rather distorted Al icosahedron. The pMC of the

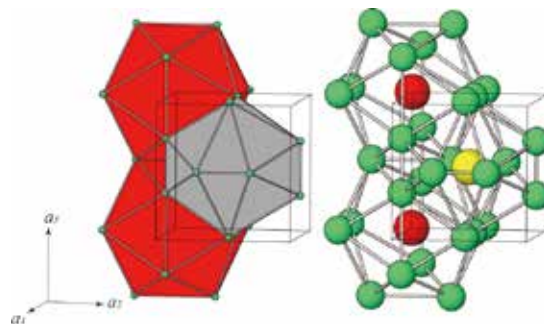


Fig. 1 Linkage of the two types of heavy metal icosahedra.

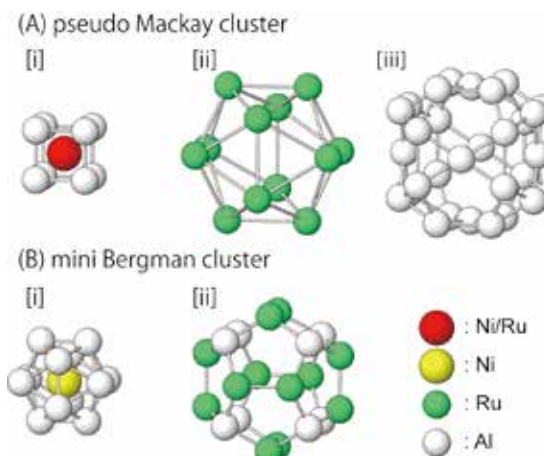


Fig. 2 Shell structure of pseudo-Mackay cluster and mini-Bergman cluster.

C-phase is categorized as pMC-A and this structural feature is attributed to the relatively Al-rich nature of the C-phase. On the contrary, the HM-rich pMC-B could be found in the structures of the C1 and C2 phases, and the unique arrangement of pMC-A and pMC-B leads to the chemical and structural variations of the 1/0 approximants.

### References

- [1] R. Simura, S. Suzuki, K. Yubuta, and K. Sugiyama, *Mater. Trans.* **54**, 1385 (2013).
- [2] K. Sugiyama, K. Yubuta, Y. Yokoyama, S. Suzuki, and R. Simura, *Acta Phys. Pol. A* **126**, 588 (2014).
- [3] R. Simura, K. Sugiyama, S. Suzuki, and T. Kawamata, *Mater. Trans.* **58**, 1101 (2017).

Keywords: X-ray diffraction (XRD), crystal structure, quasicrystal,  
 Kazumasa Sugiyama and Rayko Simura (Chemical Physics of Non-Crystalline Materials Division)  
 E-mail: kazumasa@imr.tohoku.ac.jp  
 URL: <http://www.xraylab.imr.tohoku.ac.jp/>

## Strengthening of Biomedical Co–Cr–Mo Alloys by Introducing Stacking Faults

The strengthening of biomedical Co–Cr–Mo alloys is of crucial importance to the improvement of the durability of orthopedic implants. Here, we demonstrate for the first time that a substantial increase in the number of stacking faults occurs during multipass hot deformation, resulting in a significant strengthening of the alloys.

Owing to their superior corrosion and wear resistance, Co–Cr–Mo alloys are widely used in orthopedic implants such as artificial hip joints and spinal systems. Recently, much attention has been paid to the strengthening of these alloys to improve the durability of such implants. We recently reported that a superior combination of high yield strength ( $\sim 1.5$  GPa) and good ductility ( $>10\%$ ) can be achieved by multipass hot rolling [1]. In this study, we evaluated the hot-rolled microstructures using an advanced X-ray diffraction line-profile analysis based on the extended convolutional multiple whole profile (eCMWP) fitting to analyze the relevant strengthening mechanisms [2].

Figure 1 shows the results of the eCMWP analysis of the hot-rolled specimens, plotted as a function of the applied equivalent strain ( $\varepsilon_{eq}$ ). As shown in Fig. 1(a), the dislocation density ( $\rho_{dis}$ ) first strongly increased with  $\varepsilon_{eq}$  and then became saturated to a very high dislocation density of  $8.5 \times 10^{15} \text{ m}^{-2}$  at  $\varepsilon_{eq} = 2.66$ . In contrast, the stacking fault (SF) probability ( $P_{SF}$ ) was almost zero up to  $\varepsilon_{eq} = 0.41$  and then increased sharply with further increases in  $\varepsilon_{eq}$  (Fig. 1(b)).  $P_{SF}$  was substantially higher at  $\varepsilon_{eq} = 2.66$ , reaching approximately 1.6%.

Using the eCMWP results, we ascertained the contribution of SFs ( $\sigma_{SF}$ ) to the yield stress of the prepared specimens at different values of  $\varepsilon_{eq}$  (Fig. 2). A physical model, which was proposed for hcp Mg alloys [3], was used to evaluate the SF strengthening. The  $\sigma_{SF}$  was not evident in the initial and  $\varepsilon_{eq} = 0.41$  specimens, but became significant at greater  $\varepsilon_{eq}$ . Surprisingly, the  $\sigma_{SF}$  finally reached approximately 500 MPa, which is superior to those from the other strengthening mechanisms considered. These results shed light on the importance of the SF strengthening, which has not yet been directly considered in these alloys, and will help in guiding the design and manufacturing strategy for high-strength Co–Cr–Mo alloys using lattice defects.

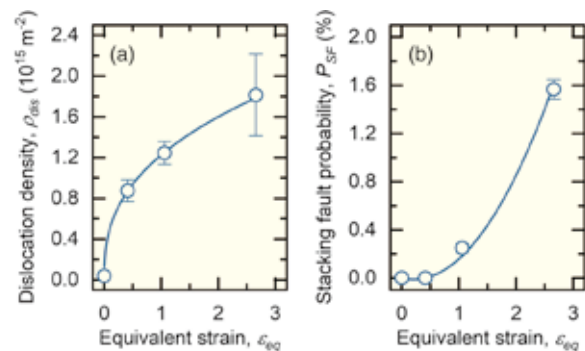


Fig. 1 Results of eCMWP analysis of the multipass hot-rolled specimens

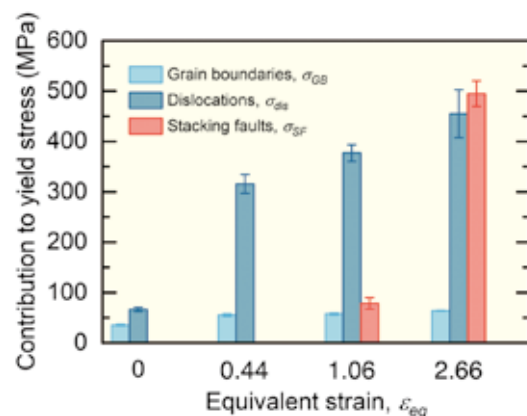


Fig. 2 Contributions of grain boundaries ( $\sigma_{GB}$ ), dislocations ( $\sigma_{dis}$ ), and stacking faults ( $\sigma_{SF}$ ) to the yield stress of the multipass hot-rolled specimens.

### References

- [1] M. Mori, K. Yamanaka, S. Sato, S. Tsubaki, K. Satoh, M. Kumagai, M. Imafuku, T. Shobu, and A. Chiba, *Acta Biomater.* **28**, 215 (2015).
- [2] K. Yamanaka, M. Mori, S. Sato, and A. Chiba, *Sci. Rep.* **8**, 10808 (2017).
- [3] W. W. Jian, G. M. Cheng, W. Z. Xu, H. Yuan, M. H. Tsai, Q. D. Wang, C. C. Koch, Y. T. Zhu, and S. N. Mathaudhu, *Mater. Res. Lett.* **1**, 61 (2013).

Keywords: alloy, defects, strength

Kenta Yamanaka and Akihiko Chiba (Deformation Processing Division)

E-mail: k\_yamanaka@imr.tohoku.ac.jp

URL: <http://www.chibalab.imr.tohoku.ac.jp/>

## Emission Characteristics of 6.78-MHz Radio-Frequency Glow Discharge Plasma in a Pulsed Mode

Boltzmann plots for atomic emission lines of iron in an argon glow discharge plasma driven by a 6.78-MHz radio-frequency (RF) voltage in a pulsed operation were investigated to discuss how the excitation/ionization process was affected by the pulsation. The excitation temperature was obtained in a narrow range of 3300–3400 K, which was hardly affected by the duty ratio of the pulsed RF glow discharge plasma.

Glow discharge optical emission spectrometry (GD-OES) is extensively employed for the direct analysis of solid samples, because the glow discharge plasma is self-sustained under a stable condition, which can provide the emission spectra with small intensity variations as well as with low background levels. GD-OES can be operated using both direct-current (DC) and radio-frequency (RF) power supplies; in particular, the latter can contribute to wider analytical applications of GD-OES, principally because it enables nonconductive samples to be analyzed. In this study [1], we selected a driving frequency of 6.78 MHz for an RF excitation source in GD-OES, mainly because it has a larger self-bias voltage than that of 13.56 MHz and thus may provide larger numbers of samples sputtered into the plasma.

The concept of local thermodynamic equilibrium (LTE) is described as follows: a plasma in the LTE state is characterized by a unique temperature that can be determined by a Maxwell-like distribution of collision partners in a dominant thermal collision of the first kind, such as collisions with energetic electrons. In this case, excitation and ionization processes occurring in the LTE plasma, resulting in the emission spectrum, could be predicted from the Boltzmann distribution among the corresponding excited energy levels. However, glow discharge plasma is not in an LTE condition and thus the excitation/ionization phenomena in GD-OES cannot be explained from the Boltzmann distribution. Our previous studies indicated that deviations from the Boltzmann distribution, which were observed in both atomic and ionic emission lines of iron, gave useful information on the excitation/ionization processes in argon GD-OES [2, 3]. In the analysis of the iron atomic lines, it was found that the excited energy levels of the iron atom above *ca.* 6 eV were more populated than a Boltzmann distribution over excitation energies of 3.4–4.6 eV, probably through stepwise de-excitation processes from higher energy levels [2].

This paper discusses Boltzmann plots for both atomic and ionic emission lines of iron, when a pulsed 6.78-MHz glow discharge plasma is employed, in comparison to the continuous RF mode. Few studies have been published regarding the plasma diagnostics of 6.78-MHz RF glow discharge in a pulsed mode. The objective of this study is to consider the Boltzmann distribution of iron emission lines in

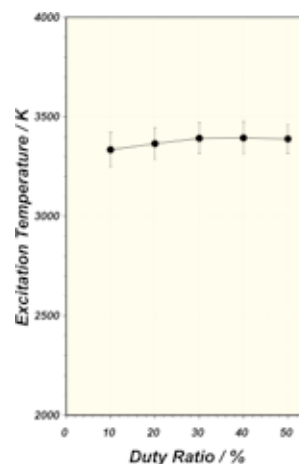


Fig. 1 Variation in the excitation temperature as a function of the duty ratio in the pulsed RF glow discharge plasma at a pulse frequency of 77 Hz.

order to understand how their characteristics can be explained by the excitation mechanism of iron species in the pulsed RF glow discharge plasma.

The excitation temperature in the pulsed RF plasma can be estimated from the slope of the linear part, the excitation energy of which ranges from 3.3 to 4.3 eV in the Boltzmann plot. Figure 1 shows a variation in the excitation temperature when different duty ratios (ratio of the power-on period to the pulse width) are selected at a pulse frequency of 77 Hz in an Ar plasma of 530 Pa, and then the excitation temperature became almost unchanged (*ca.* 3350 K), whereas the net emission intensities were drastically reduced at lower duty ratios. This effect implied that a glow discharge plasma could be sustained by a self-stabilized negative glow zone in which the kinetic energy of the electron would be hardly changed under a uniform potential distribution, thus determining the excitation of iron atoms principally.

### References

- [1] X. Zhang and K. Wagatsuma, *Spectrochim. Acta Part B* **133**, 72 (2017).
- [2] L. Zhang, S. Kashiwakura, and K. Wagatsuma, *Spectrochim. Acta Part B* **66**, 785 (2011).
- [3] L. Zhang, S. Kashiwakura, and K. Wagatsuma, *Spectrochim. Acta Part B* **67**, 24 (2012).

Keywords: atomic emission spectrometry, glow discharge plasma, plasma diagnostic  
 Kazuaki Wagatsuma (Analytical Science Division)  
 E-mail: [wagatsuma@imr.tohoku.ac.jp](mailto:wagatsuma@imr.tohoku.ac.jp)  
 URL: <http://wagatsuma.imr.tohoku.ac.jp/>

## Preparation of Bioactive Porous Surfaces in Biomedical Co-Cr-Mo Alloy

Nano- or submicron porous surfaces can significantly enhance cell attachment, which accelerates the formation of new bone tissue. We recently presented a novel method for preparing such porous surfaces in biomedical Co-Cr-Mo alloy, which involves local dealloying in a pure Zn melt and selective removal of the Zn-rich phase formed in the dealloying products.

Biomedical Co-Cr-Mo (CCM) alloys have been widely used in orthopedic implants such as artificial knee and hip joints. Nevertheless, they are considered inferior to Ti-based alloys in terms of osseointegration and bone anchorage, for which chemical and electrochemical methods are generally utilized for introducing nano/submicron porous surface structures.

We designed a novel method to prepare Zn-incorporated nano/submicron porous surface structures in CCM alloy by a combination of local dealloying and selective dissolution [1]. First, a reaction layer was formed by a dealloying reaction of CCM alloy in Zn melt, which was significantly affected by the dealloying temperature and period. Co in the alloy was selectively dealloyed, and dispersoids and filamentary structures were formed, which grew vertically from the CCM matrix, as shown in Fig. 1(a).

Two types of phases with different compositions are evident; one phase is rich in Co and Zn (Zn-rich phase), and the other phase is rich in Co and Cr (Zn-lean phase). According to Figs. 1(a) and 1(b), the compositions of the Zn-rich and Zn-lean phases are Co-Cr<sub>2.3-2.8</sub>-Mo<sub>0.3-0.8</sub>-Zn<sub>45-47</sub> (wt.%) and Co-Cr<sub>36-39</sub>-Mo<sub>8-10</sub>-Zn<sub>4-9</sub> (wt.%). A portion of the Zn atoms diffused into the CCM matrix and formed a compound of Co-Cr<sub>22</sub>-Mo<sub>2.6</sub>-Zn<sub>9.7</sub> (wt.%).

Homogeneous porous structures are produced by selectively dissolving the Zn-rich phase, as shown in Fig. 1(c). The pores are on the submicron-scale, and the thickness of the porous structure is approximately 4  $\mu\text{m}$ . The bioactivity of CCM alloy is expected to be improved by the porous surfaces introduced in present study, because the rough surfaces generally resulted in enhanced cell attachment onto biomaterial surfaces.

### References

[1] D. Wei, Y. Koizumi, and A. Chiba, *Mater. Lett.* **219**, 256 (2018).

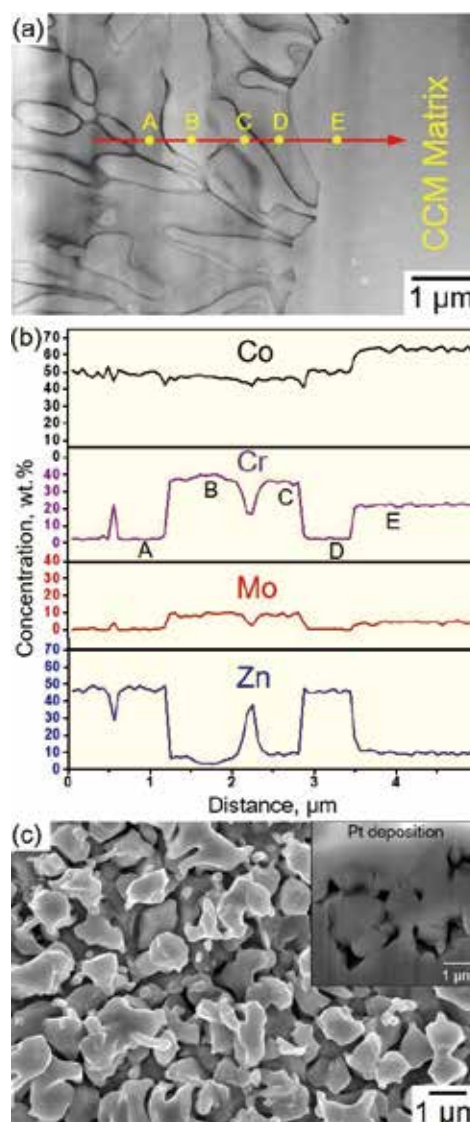


Fig. 1(a) Cross-sectional STEM-HAADF (high-angle angular dark field scanning transmission electron microscopy) image of CCM alloy dealloyed in a pure Zn melt at 800 °C for 5 h; (b) corresponding EDS (energy dispersive X-ray spectrometry) line scan along the red arrow; (c) SEM (scanning electron microscope) image of CCM alloy surface after dealloying in pure Zn melt and subsequent selective dissolution [1].

Keywords: surface reaction, nanostructure, corrosion

Daixiu Wei (Creation of Life Innovation Materials for Interdisciplinary and International Researcher Development)

E-mail: wei1987xiu@imr.tohoku.ac.jp

URL: <http://life-pro.imr.tohoku.ac.jp/index.html>

## *Energy-Related Materials*

IMR KINKEN Research Highlights 2018



## Origin of Resistance at Si/GaAs Heterointerfaces for Tandem Solar Cells Fabricated by Surface-Activated Bonding at Room Temperature

The intrinsic microstructure of Si/GaAs heterointerfaces for tandem solar cells, fabricated by surface-activated bonding at room temperature, is examined. The bonded heterointerfaces include an arsenic-deficient crystalline GaAs layer and an amorphous Si layer of approximate thicknesses less than 1 nm and 3 nm, respectively, introduced by the irradiation of an argon atom beam for surface activation before bonding. It is hypothesized that the intrinsic interface resistance mainly originates from the arsenic-deficient defects in the former layer.

Tandem solar cells consisting of silicon (Si) and III-V compounds are one of the promising candidates for next-generation terrestrial photovoltaic systems, which can surpass the efficiency milestone of 30% for non-concentrating solar cells without using expensive Ge or GaAs substrates. Recently, as a low-cost process, surface-activated bonding (SAB) at room temperature (RT), in which the surfaces of substrates are activated before bonding by creating dangling bonds via the removal of contaminants under an energetic particle bombardment in high vacuum (using an argon fast atom beam), has been applied to form Si/GaAs heterointerfaces for hybrid triple-junction solar cells with a high conversion efficiency above 26% [1]. Even though the interface resistance ( $\sim 10^{-1} \Omega\text{cm}^2$ ) is low enough for solar cells, it is still higher than the ideal value at defect-free heterointerfaces ( $\sim 10^{-4} \Omega\text{cm}^2$ ). A comprehensive understanding of the electrical properties at the heterointerfaces depending on their atomic structure is indispensable to establish low-cost fabrication processes of high-efficiency tandem solar cells by optimizing the interface structure.

In the present work [2], we examined the Si/GaAs heterointerfaces fabricated at RT under a SAB condition [1], with the substrates of B-doped (100) p-type Si (with a carrier concentration of  $2 \times 10^{14} \text{ cm}^{-3}$ ) and Si-doped (100) n-type GaAs ( $2 \times 10^{16} \text{ cm}^{-3}$ ) which was  $5^\circ$  off from (001) toward [110]. Some of them were then annealed at 673 K for 1 min. The structural properties were determined by transmission electron microscopy (TEM).

As-bonded heterointerfaces included an arsenic-deficient crystalline GaAs layer less than approximately 1 nm thick and an amorphous Si layer of approximate thickness 3 nm. Dimples were introduced on the entire GaAs surface at the bonding heterointerface, via the introduction of arsenic vacancies during the surface activation process, and they disappeared after annealing at 673 K. Moreover, small number of dislocations due to

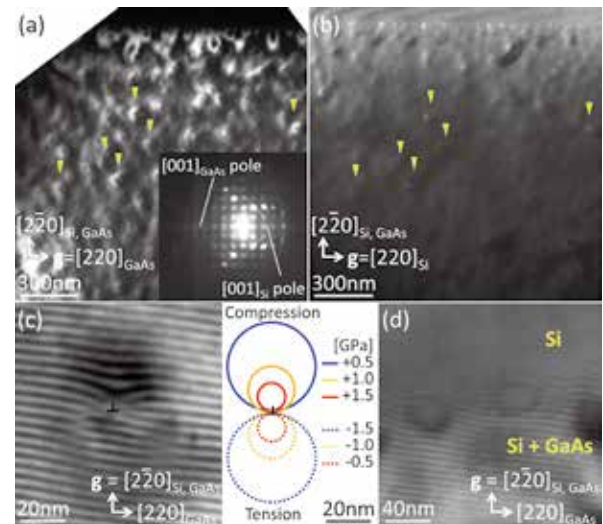


Fig. 1 Dark-field TEM of (a) GaAs and (b) Si at a heterointerface taken with the (220) reflection for GaAs and Si, respectively. The inset in (a) shows the corresponding electron diffraction. (c, d) Bright-field TEM of the interface taken with both the (2-20) reflections for Si and GaAs due to (c) a dislocation in GaAs cropping out the interface and (d) arsenic-deficient dimples on the GaAs surface. The inset in (c) indicates the calculated hydrostatic stress field for dislocations in GaAs.

dislocations existed on the surface. The density in the amorphous Si layer was lower than in the conventional amorphous Si, owing to the introduction of Si vacancies during the surface activation process, and it was recovered by annealing at 673 K. The interface resistance can be reduced by suppressing those defects via the optimization of SAB conditions.

### References

- [1] N. Shigekawa, J. Liang, R. Onitsuka, T. Agui, H. Juso, and T. Takamoto, *Jpn. J. Appl. Phys.* **54**, 08KE03 (2015).
- [2] Y. Ohno, H. Yoshida, S. Takeda, J. Liang, and N. Shigekawa, *Jpn. J. Appl. Phys.* **57**, 02BA01 (2018).

Keywords: solar cells, defects, interface

Yutaka Ohno (Physics of Crystal Defects Division)

E-mail: yutakaohno@imr.tohoku.ac.jp

URL: <http://lab-defects.imr.tohoku.ac.jp>

## Direct Observation of Deuterium Trapping at Irradiation-Induced Vacancy Clusters in Tungsten by Positron Annihilation Spectroscopy

Deuterium trapping at vacancy clusters in neutron-irradiated tungsten, a primary candidate material for plasma-facing components in fusion reactors, was revealed by positron annihilation spectroscopy. This is the first direct observation of the potential origin of the significant increase in hydrogen retention in irradiated tungsten.

The development of fusion reactors such as International Thermonuclear Experimental Reactor (ITER) has been improving. In plasma-facing components, energetic hydrogen is induced together with radiation damage due to exposure to fusion plasma. Because tritium is an essential fusion reaction source, it is necessary to constrain its retention in the plasma-facing components. Such constraints are also of great importance from a safety perspective. Tungsten is a primary candidate material for the plasma-facing components, owing to its high melting point and high sputtering resistance to energetic particles. The solubility of tritium in tungsten is very low (the lowest among metals), which is an advantage in reducing tritium retention during the operation of fusion reactors. However, recent studies have reported that irradiation causes significant enhancement of hydrogen retention in tungsten. This is ascribed to hydrogen trapping at irradiation-induced defects such as vacancies and vacancy clusters; however, it has not yet been clarified. We employed positron annihilation spectroscopy (PAS) to reveal both irradiation-induced defects and hydrogen in neutron-irradiated tungsten [1].

Pure tungsten (4N) was neutron-irradiated at  $\sim 573$  K for  $\sim 40$  days to the dose of  $\sim 0.3$  dpa, followed by post-irradiation annealing (PIA) at 573 K for 100 hours. The PIA was performed under vacuum or in deuterium gas at  $\sim 0.1$  MPa. In the as-irradiated state, the formation of vacancy clusters with the size of  $\sim V_{40}$  was revealed by positron lifetime measurements. After the PIA in vacuum, the positron lifetime was almost the same as that in the as-irradiated state, indicating no change in the vacancy clusters. However, after the PIA in deuterium gas, the positron lifetime was significantly shorter than that in the as-irradiated state, strongly suggesting positron annihilation with deuterium electrons at the vacancy clusters. To analyze the chemical environment at the positron trapping sites, coincidence Doppler broadening (CDB) measurements were performed. Figure 1 shows the correlation between the low- and high-momentum fractions in the CDB spectra. It should be noted that the correlation point for the PIA in deuterium, shown as a red point, was not located on the dashed line connecting the unirradiated and as-irradiated states. This clearly indicates positron annihilation with deuterium electrons, and thus deuterium trapping at irradiation-induced vacancy clusters was revealed. This gives the first direct observation of deuterium trapping at irradiation-induced defects, which is suggested to be the main origin of the significant increase in hydrogen isotope retention in irradiated tungsten.

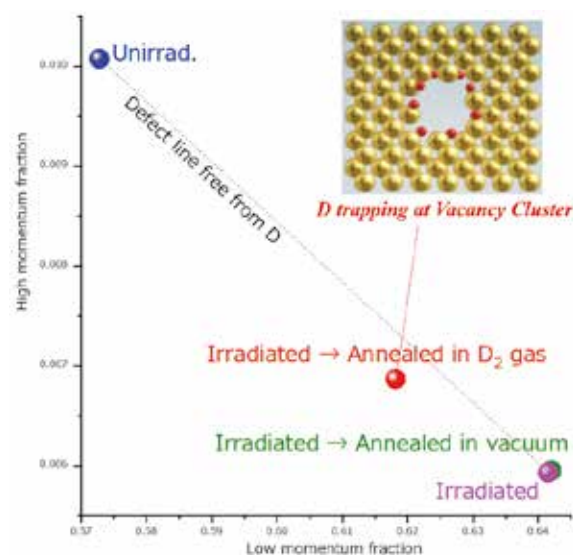


Fig. 1 Correlation of low- and high-momentum component fractions of CDB measurements for neutron-irradiated pure tungsten.

measurements were performed. Figure 1 shows the correlation between the low- and high-momentum fractions in the CDB spectra. It should be noted that the correlation point for the PIA in deuterium, shown as a red point, was not located on the dashed line connecting the unirradiated and as-irradiated states. This clearly indicates positron annihilation with deuterium electrons, and thus deuterium trapping at irradiation-induced vacancy clusters was revealed. This gives the first direct observation of deuterium trapping at irradiation-induced defects, which is suggested to be the main origin of the significant increase in hydrogen isotope retention in irradiated tungsten.

### References

- [1] T. Toyama, K. Ami, K. Inoue, Y. Nagai, K. Sato, Q. Xu, and Y. Hatano, *J. Nucl. Mater.* **499**, 464 (2018).

Keywords: positron annihilation, nuclear materials, vacancy

Yasuyoshi Nagai, Koji Inoue, Yasuo Shimizu, and Kazuaki Nagumo (Irradiation Effects in Nuclear and Their Related Materials Division)

E-mail: nagai@imr.tohoku.ac.jp

URL: <http://wani.imr.tohoku.ac.jp/>

## Three-Dimensional Imaging of Threading Dislocations in GaN Using Multiphoton-Excitation Photoluminescence

Three-dimensional imaging of threading dislocations in GaN was demonstrated by using multiphoton-excitation photoluminescence. Threading dislocations have nonradiative characteristics, and thus these are visualized as dark lines in the photoluminescence images. This can be considered as a novel method for characterizing defects in GaN films without any destructive preparations.

Nitride semiconductors have been widely used for the applications of optoelectronic devices, such as blue light-emitting diodes, violet laser diodes, and high-electron-mobility transistors. Recently, the GaN-based vertical devices have attracted much attention for hybrid and electric vehicles. These vehicles require power electronics to drive high-power motors. GaN-based vertical transistors can achieve both high breakdown voltage larger than 1 kV and low on-resistance. Because these properties are superior to the current electronic devices based on Si, GaN-based vertical devices are expected for power electronics. For fabricating GaN-based power devices, a GaN wafer with low defect density is indispensable. Currently, a GaN wafer has been fabricated from a thick GaN film grown on a foreign substrate. The density of threading dislocations (TDs) in a GaN depends on the growth method, growth conditions, and the thickness. To achieve many fewer TDs in bulk GaN, it is important to clarify how TDs propagate in GaN crystal. In this study, multiphoton-excitation photoluminescence, which does not require special sample preparation, is proposed to analyze the three-dimensional distribution of TDs in GaN.

Unintentionally doped *n*-type *c*-plane GaN templates, which are grown by halide vapor phase epitaxy on a sapphire substrate, are used for the measurement of TDs. A Ti: Sapphire laser with a wavelength of 700 nm was used as an excitation source. The laser beam was focused into the interior of the sample with an objective lens. Photoluminescence occurs at the focal point in GaN, and it is extracted from the sample. Only a near-band-edge emission of GaN is corrected by using a bandpass filter and it is detected with a photomultiplier tube. Three-dimensional photoluminescence images are obtained by scanning the focal point of the laser beam in the in-plane and depth directions.

The in-plane photoluminescence image measured at a fixed focal depth showed dark spots,

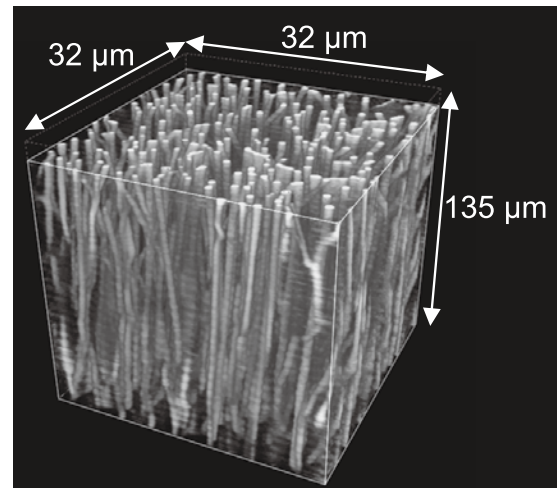


Fig. 1 Three-dimensional photoluminescence image of GaN. Contrast is inverted: dark lines are shown as bright.

which corresponded to TDs. The diameter of the dark spots was approximately  $0.6 \mu\text{m}$ , which was determined by the diffusion length of minority carriers in the sample. The distribution of dark spots in the in-plane image changed with the focal depth. The three-dimensional images were constructed by stacking the depth-dependent in-plane images, as shown in Fig. 1 [1]. All the dark spots connected to form dark lines in the three-dimensional image. This reflects the propagation behavior of the TDs. By comparing the TD density, the thickness dependence of the TD density can be obtained. The densities of TDs at the depths of  $0 \mu\text{m}$  (surface),  $50 \mu\text{m}$ , and  $100 \mu\text{m}$  were  $6.6 \times 10^7$ ,  $8.0 \times 10^7$ , and  $1.2 \times 10^8 \text{ cm}^{-2}$ , respectively. The change in the TD density showed the annihilation properties of TDs during the crystal growth.

It can be concluded that this method is powerful for characterizing defects in GaN films.

### References

- [1] T. Tanikawa, K. Ohnishi, M. Kanoh, T. Mukai, and T. Matsuoka, *Appl. Phys. Express* **11**, 031004 (2018).

Keywords: 3D structure, optical properties, defects  
Takashi Matsuoka (Physics of Electronic Materials Division)  
E-mail: [matsuoka@imr.tohoku.ac.jp](mailto:matsuoka@imr.tohoku.ac.jp)  
URL: <http://www.matsuoka-lab.imr.tohoku.ac.jp/?TOPPAGE>

## Toward Constructing Novel Rechargeable Battery Using Mg Cation

We are currently constructing a new type of rechargeable battery using divalent Mg cation as one topic of our laboratory. Recently, we have found that Mg insertion into spinel lattices occurs via an “intercalation and push-out” process to form a rocksalt phase in the spinel mother phase. For example, by utilizing the valence change from Co(III) to Co(II) in  $\text{MgCo}_2\text{O}_4$ , the Mg insertion occurs at a considerably high potential of approximately 2.9 V vs.  $\text{Mg}^{2+}/\text{Mg}$ , being comparable to the ab initio calculation.

In terms of energy and environmental concerns, modern industrial society strongly demands high-energy-density rechargeable storage batteries. Currently, lithium ion batteries (LIBs) are widely used for many practical applications, and their energy density has been enlarged year by year, but this growth rate has recently tended to saturate. If lithium metal itself could be used as an anode material, instead of the currently used carbonaceous materials, LIBs would have shown significantly high energy densities. However, this is difficult at present, owing to the well-known fatal problem, “dendritic growth” of Li metal on charging that leads to dangerous short circuits. Therefore, to further enhance the energy density of storage batteries, we must develop new types of metal-anode battery systems.

As an alternative to Li metal-anode batteries, polyvalent-metal storage batteries have attracted increased attention owing to their large capacities; for example, in the case of Mg, its capacity ( $\sim 2200 \text{ mAhg}^{-1}$ ) greatly exceeds that of the current carbonaceous anode materials ( $\sim 370 \text{ mAhg}^{-1}$ ). In particular, Mg electrodeposition tends to occur with nondendritic formation; therefore, Mg metal can be expected to work as an anode material. However, Mg rechargeable battery (MRB) research is still a very challenging and unestablished field. Unless high-performance cathode materials are sought out, MRBs would not be comparable to LIBs in terms of energy density. Thus, to alter the energy storage paradigm, we must seek cathode materials for polyvalent cations.

With several magnesium spinel oxides,  $\text{MgCo}_2\text{O}_4$ ,  $\text{MgMn}_2\text{O}_4$ ,  $\text{MgFe}_2\text{O}_4$ ,  $\text{MgCr}_2\text{O}_4$ , and  $\text{Co}_3\text{O}_4$ , we demonstrated that some of the spinel oxides can allow the insertion of Mg cations at high potentials ( $\sim 3 \text{ V}$  vs.  $\text{Mg}^{2+}/\text{Mg}$ ) via an “intercalation and pushout” mechanism in Figs. 1a–1d. Figure 1e shows the results of the cathode performance test [1]. Based on these significant results, we are now trying to construct a new type of dual-carrier battery using Li and Mg cations [2].

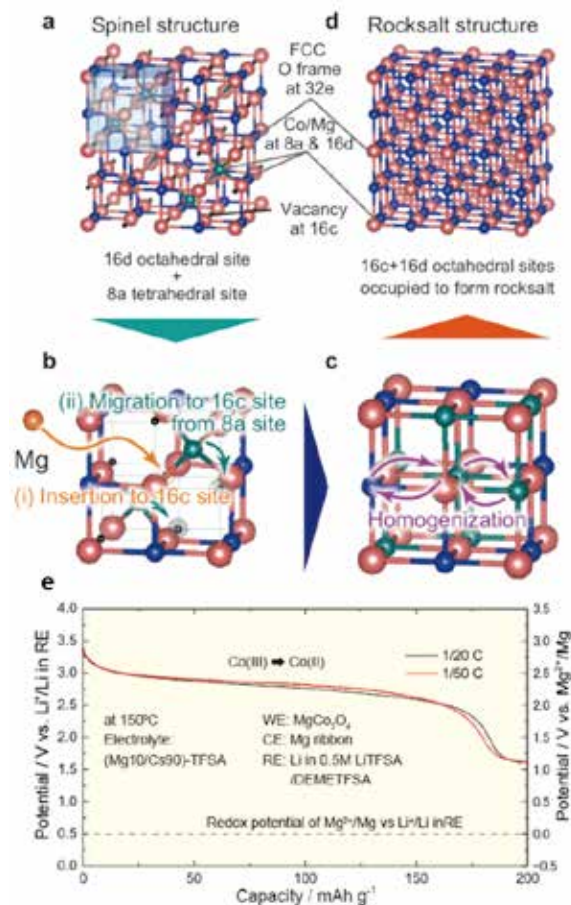


Fig. 1 (a–d) Schematic figure illustrating the insertion mechanism of Mg cations into the spinel lattice. (e) Discharge test using the  $\text{MgCo}_2\text{O}_4$  cathode material.

### References

- [1] S. Okamoto, T. Ichitsubo, T. Kawaguchi, Y. Kumagai, F. Oba, S. Yagi, K. Shimokawa, N. Goto, T. Doi, and E. Matsubara, *Adv. Sci.* **2**, 1500072 (2015).
- [2] H. Li, T. Ichitsubo, S. Yagi, and E. Matsubara, *J. Mater. Chem. A* **5**, 3534 (2017).

Keywords: energy storage, oxide, crystal structure

Tetsu Ichitsubo (Structure-Controlled Functional Materials Division)

E-mail: tichi@imr.tohoku.ac.jp

URL: <http://ilab.imr.tohoku.ac.jp/index.html>

## Effect of the Cooling Rate on the Mechanical Properties of Ti-Ni-Cu-Zr-Based Glassy/Crystalline Alloys

Ti-Ni-Cu-Zr-based glassy-crystalline dual-phase alloy samples with different sizes and good mechanical properties were manufactured. Their deformation curves had a double sigmoidal shape with three deformation stages. The interplay between dislocation slip and shear deformation of the homogeneous dual-phase structure contributed the good combination of strength and ductility, in conjunction with the superelastic behavior and the transformation-induced plasticity effect during martensitic transformation.

The glassy-crystalline dual-phase of bulk metallic glass composites (BMGCs) emerged at the end of the 20<sup>th</sup> century to overcome the sudden fracture of bulk metallic glasses (BMGs) [1]. The present work investigates the cooling rate effect on Y-, Co-, and Nb-containing Ti-Ni-Cu-Zr-based BMGCs. The cooling rate has a significant impact on the formation of the glassy phase as well as the deformation behavior via different casting diameters (2 mm, 3 mm, and 5 mm) of cylindrical specimens (length: 50 mm) [2].

Figure 1(a) was taken from the polished cross-sectional surface of the as-cast 3-mm diameter Ti<sub>40</sub>Ni<sub>39.5</sub>Cu<sub>8</sub>Zr<sub>10</sub>Co<sub>2</sub>Y<sub>0.5</sub> alloy. The alternating glassy and crystalline phases form the homogeneous net-like structure.

The mechanical properties are shown in Fig. 1(b). The specimens were deformed to a fairly large strain of 20% and tolerated a high stress of 2500 MPa prior to fracture. The structures of the Ti-Ni-Cu-Zr based alloys contain a glassy phase with a cP2 (Pearson symbol)-type crystalline phase. This cP2-TiNi phase coincides with the high-temperature austenitic phase, which may transform into the low-temperature martensitic mP4-phase at relatively low stresses. Furthermore, unlike the serrated plastic flow typical for BMGs, the massive shear banding behavior was prevented. Additionally, catastrophic failure was delayed.

The crystalline phases act as obstacles to shear band propagation and, in conjunction with the superelastic and transformation-induced plasticity (TRIP) effects, induce ductility and strength enhancement. Higher fractions of the mP4 phase occur in the larger samples (lower cooling rate) than in their smaller counterparts. The relatively slow cooling rate of the large samples promotes equilibrium-phase formation.

The three stages in the work-hardening curves correspond to (I) elastic deformation, (II) stress-induced martensitic transformation, and (III) plastic

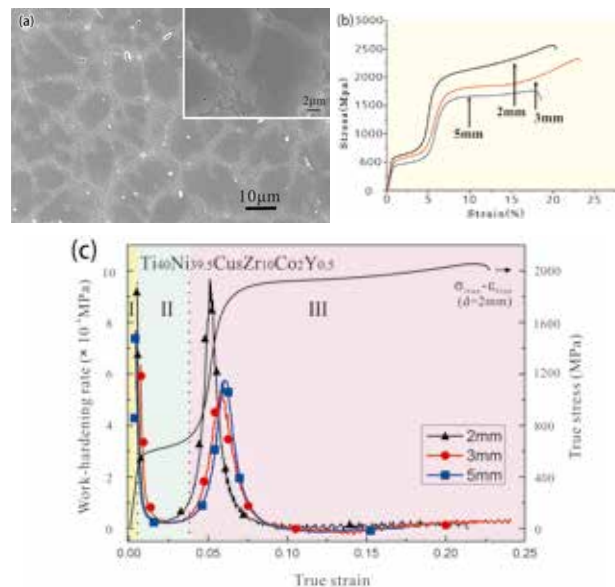


Fig. 1 (a) SEM images of the polished cross-section of Ti<sub>40</sub>Ni<sub>39.5</sub>Cu<sub>8</sub>Zr<sub>10</sub>Co<sub>2</sub>Y<sub>0.5</sub> alloy. (b) Compressive stress–strain curves. (c) Curves showing the work-hardening rate with different diameters.

deformation (Fig. 1(c)). The martensitic transformation is reversible and, hence, the elastic transformation is constrained by the amorphous matrix and dislocation, and shear band propagation is difficult. Therefore, the martensitic transformation (stage II) finishes earlier in the 2-mm-diameter sample, which contains a larger fraction of the amorphous phase. The work-hardening rate increases at the plastic deformation (stage III), and the strain–stress curves plateau with increasing volume fraction of the martensitic phase.

### References

- [1] C. C. Hays, C. P. Kim, and W. L. Johnson, Phys. Rev. Lett. **84**, 2901 (2000).
- [2] J. Jiang, S. Ketov, H. Kato, and D. V. Louzguine-Luzgin, Mater. Sci. Eng. A **704**, 147 (2017).

Keywords: bulk metallic glass, deformation, mechanical properties  
 Hidemi Kato (Non-Equilibrium Materials Division)  
 E-mail: hikato@imr.tohoku.ac.jp  
 URL: <http://www.nem.imr.tohoku.ac.jp>

## Nine Hydrogen Atoms Binding to Transition Metals

Nine-fold hydrogen (H-) coordination is very rare, and has been observed only in two different transition-metal hydride complexes comprising Group 7 elements, rhenium ( $[\text{ReH}_9]^{2-}$ ) and technetium ( $[\text{TcH}_9]^{2-}$ ). Here, we introduce our recent findings in the exploration of novel nine-fold H-coordination hydride complexes.

Despite having the simplest form of any element, hydrogen has an exceptionally rich chemistry, forming various chemical bonds in materials. It is the source of many functionalities in hydrides; thus, materials containing a large amount of hydrogen could be promising candidates for the emergence of latent functionalities [1].

Complex transition-metal hydrides represent a class of hydrogen-rich materials, wherein a number of H atoms covalently bind to transition metals to form a varied set of hydride complexes with a rich variety of H-coordination modes. At the same time, nine-fold H-coordination is very rare, and has been observed only in the Group 7 hydride complexes,  $[\text{ReH}_9]^{2-}$  and  $[\text{TcH}_9]^{2-}$ .

In this regard, by means of a combined theoretical and experimental approach, we have explored other nine-fold H-coordination hydride complexes. Our density functional theory (DFT) calculations predicted that a tricapped trigonal prismatic H-coordination allows the formation of Group 5 and 6 hydride complexes of  $[\text{NbH}_9]^{4-}/[\text{TaH}_9]^{4-}$  and  $[\text{MoH}_9]^{3-}/[\text{WH}_9]^{3-}$  in  $\text{Li}_6\text{NbH}_{11}/\text{Li}_6\text{TaH}_{11}$  and  $\text{Li}_5\text{MoH}_{11}/\text{Li}_5\text{WH}_{11}$ , respectively, as shown in Fig. 1. The prediction is strongly supported by X-ray diffraction (XRD) and Raman spectroscopic measurements of the samples prepared by a high-pressure and high-temperature (HPHT) technique [2].

Furthermore, from the results of first-principles molecular dynamics (FPMD) calculations and neutron diffraction (ND) measurements of the deuteride analogue,  $\text{Li}_5\text{MoD}_{11}$ , we found that the nine-fold H-coordination hydride complexes exhibit significant rotations at room temperature, as depicted in the inset of Fig. 2(b). This is strongly reminiscent of the reorientation jumps of *closo*-polyboranes observed in alkali-metal *closo*-polyborane salts, which are often discussed in relation to the translational diffusion of alkali metals. As such, the emergence of fast lithium ion conduction may be expected in the present materials, even at room temperature.

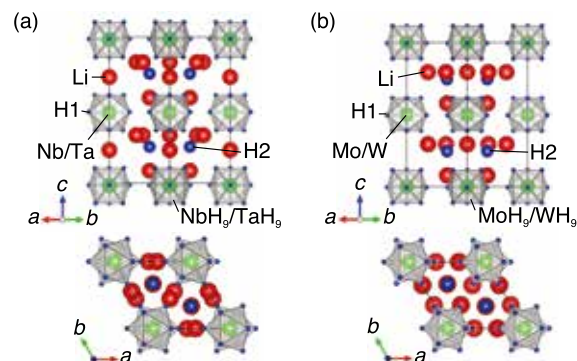


Fig. 1 DFT structures of (a)  $\text{Li}_6\text{NbH}_{11}/\text{Li}_6\text{TaH}_{11}$  and (b)  $\text{Li}_5\text{MoH}_{11}/\text{Li}_5\text{WH}_{11}$ .

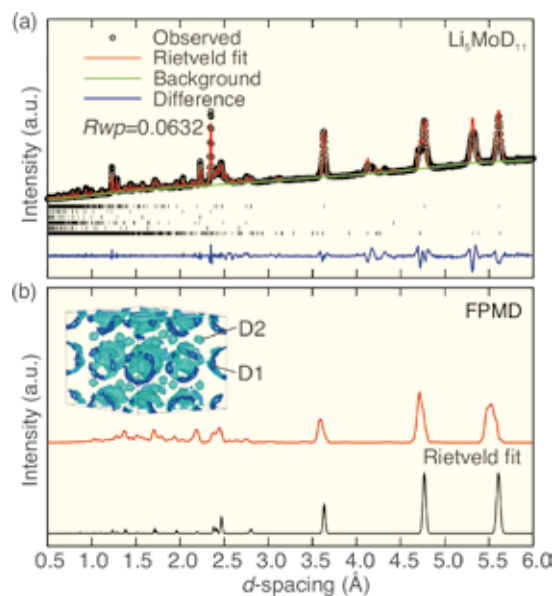


Fig. 2 ND profiles. (a) Experimental profile of  $\text{Li}_5\text{MoH}_{11}$  measured at room temperature. (b) Simulated profile from FPMD trajectory at 298 K (red line) and Rietveld fit of experimental profile (black line). The inset depicts the time-averaged atomic-density profile from the FPMD trajectory of D atoms at 298 K, showing the occurrence of significant rotations of the hydride complexes.

### References

- [1] S. Takagi and S. Orimo, *Scr. Mater.* **109**, 1 (2015).
- [2] S. Takagi, Y. Iijima, T. Sato, H. Saitoh, K. Ikeda, T. Otomo, K. Miwa, T. Ikeshoji, and S. Orimo, *Sci. Rep.* **7**, 44253 (2017).

Keywords: hydride, first-principles calculations, crystal structure  
 Shigeyuki Takagi and Shin-ichi Orimo (Hydrogen Functional Materials Division)  
 E-mail: shigeyuki.takagi@imr.tohoku.ac.jp  
 URL: <http://www.hydrogen.imr.tohoku.ac.jp/index.html>

## Growth of Metals and Alloys by the A- $\mu$ -PD Method

An innovative method acceptable for the production of iridium (Ir) and ruthenium (Ru) metal fibers with high melting point and poor workability is developed using an alloy-micro-pulling-down (A- $\mu$ -PD) method. Both Ir and Ru fibers were composed of number of elongated grains oriented along the growth direction, which is attributable to the unidirectional solidification.

In the case of wire-shaped products, Ir and Ir-alloy wires have been made from Ir columnar ingots by multiple hot-working processes using dies with holes of the intended diameter. However, such hot-working processes increase the manufacturing cost owing to the yield loss, especially for metals and alloys with difficult workability such as Ir and its alloys. In addition, the manufacturing cost increases as a result of losses of starting materials and increases in labor cost in the working processes.

In this report, Ir and Ru fibers with poor workability were grown from the melt by the A- $\mu$ -PD method [1]. The key differences between the A- $\mu$ -PD method and traditional  $\mu$ -PD method are associated with the crucible design, heating of starting materials, and pulling-down system. The growths were performed from dense-pour ZrO<sub>2</sub> crucibles with high mechanical strength and thermal shock resistance. An Ir fiber exceeding 15 m in length was grown using a pinch-roller (Fig. 2). The as-grown Ir and Ru fibers were composed of elongated grains that demonstrated aligned crystal orientations along to the growth direction. The flexibility of the Ir fiber grown by the A- $\mu$ -PD method was considerably improved as compared to a commercial Ir wire made by a wire-drawing process. This improvement in flexibility is associated with the elongated grains. Therefore, the A- $\mu$ -PD method can be used for improvement in mechanical and chemical properties of the grown fibers, in addition to the innovative growth of the fibers of metals and alloys with poor workability. Fabrication by the A- $\mu$ -PD method will be applied to the development of various functional metals and alloys in our future work.

For example, Fe-Ga alloy polycrystals subject to cross-sectional shape control, such as fiber and plate shape, were successfully grown using the A- $\mu$ -PD method [2]. A prototype vibration energy harvester showed good performance comparable to or greater than the device using commercially available Fe-Ga alloys. Despite the need to improve the crystal orientation, leveraging the advantages of

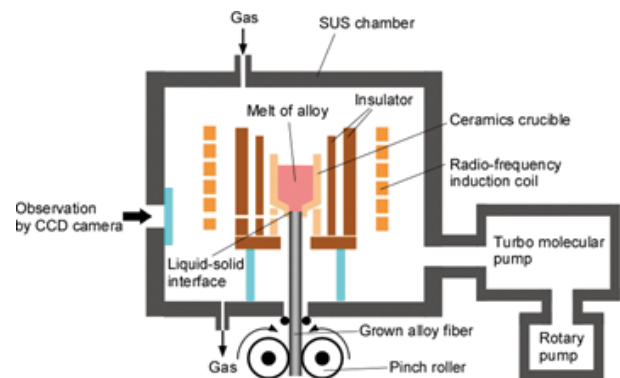


Fig. 1 Schematic diagram of the developed A- $\mu$ -PD apparatus.

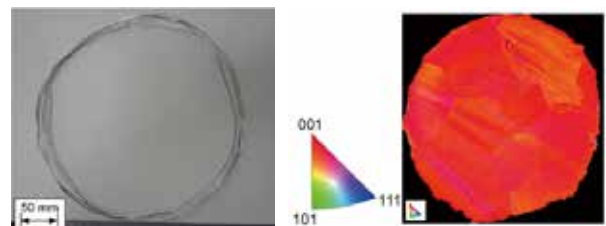


Fig. 2 Ir fiber grown by the A- $\mu$ -PD method and EBSD image of a cross-sectional plane of the Ir fiber.

the near net-shape controlling and a growth rate vastly superior to other crystal growth techniques is expected to underline the role of the shape-controlled  $\mu$ -PD method as a promising technique for the mass-production of Fe-Ga alloys as energy harvester application materials.

### References

- [1] Y. Yokota, T. Nihei, K. Tanaka, K. Sakairi, V. Chani, Y. Ohashi, S. Kurosawa, K. Kamada, and A. Yoshikawa, *Adv. Eng. Mater.* **20**, 1700506 (2018).
- [2] M. Ito, K. Kamada, A. Yoshikawa, T. Kawamata, S. Fujieda, S. Suzuki, T. Minamitani, and T. Ueno, *J. Alloys Compd.* **731**, 898 (2018).

Keywords: crystal growth, metal, alloy

Akira Yoshikawa (Advanced Crystal Engineering Laboratory)

E-mail: yoshikawa@imr.tohoku.ac.jp

URL: <http://yoshikawa-lab.imr.tohoku.ac.jp/index-e.html>

## Laser Chemical Vapor Deposition of Photocatalytic Perovskite Films

Photocatalytic NaTaO<sub>3</sub>, SrZrO<sub>3</sub>, and SrTiO<sub>3</sub> perovskite films were prepared by laser chemical vapor deposition (LCVD). The (001) oriented orthorhombic NaTaO<sub>3</sub> film showed hydrogen evolution at a rate of 5672 mol g<sup>-1</sup> h<sup>-1</sup> upon irradiating with a 254-nm UV light. The solar to hydrogen conversion efficiency of the NaTaO<sub>3</sub> film is 1.93%, almost three times higher than the previously reported value.

Perovskite-related compounds such as SrTiO<sub>3</sub>, SrZrO<sub>3</sub>, and NaTaO<sub>3</sub> are promising photocatalytic materials for water-splitting under ultraviolet light. In earlier studies, these films were prepared by wet chemical route and flux coating. However, it is difficult to control the orientations and morphology of these films by wet chemical routes. The photocatalytic activity is strongly affected by the crystallinity and crystal orientation of such perovskite films. A highly crystalline and oriented film is required for high photocatalytic activity. Further, it normally takes hours to prepare films, which significantly inhibits the synthesis efficiency. Physical vapor deposition (PVD) and chemical vapor deposition (CVD) have been widely used to prepare both thin and thick films. However, it is very difficult to control the composition of alkaline and alkaline-earth elements, particularly Na composition, in the films because of the volatility and instability of Na. No study has so far reported the use of either PVD or CVD method to prepare NaTaO<sub>3</sub> and SrZrO<sub>3</sub> films.

Laser CVD is an advantageous method to prepare oxide films as it allows the control of phases, significant orientations, and morphologies at a very high deposition rate. The SrTiO<sub>3</sub>, NaTaO<sub>3</sub>, and SrZrO<sub>3</sub> films were prepared on polycrystalline AlN substrates. A continuous wave of Nd:YAG laser (wavelength: 1064 nm) was employed at a laser output of 10–150 W. The substrate was heated on a heating stage at a pre-heating temperature of 873 K. The Na(dpm), Sr(dpm)<sub>2</sub>, Ti(O-*i*-C<sub>3</sub>H<sub>7</sub>)<sub>2</sub>(dpm)<sub>2</sub>, and Ta(O-*i*-C<sub>3</sub>H<sub>7</sub>)<sub>5</sub> were used as precursors. The total pressure in the CVD chamber was held at 800 Pa. The deposition process was conducted for 600 s.

Figure 1 shows the surface and cross-sectional scanning electron microscopy (SEM) images of NaTaO<sub>3</sub> films prepared at  $T_{\text{dep}} = 793$  K (Fig. 1(a) and (c)) and 853 K (Fig. 1(b) and (d)) [1]. The (001)-oriented orthorhombic NaTaO<sub>3</sub> film prepared at  $T_{\text{dep}} = 793$  K had a columnar cross-section with a tilted roof-like surface. The (100)-oriented monoclinic NaTaO<sub>3</sub> film prepared at  $T_{\text{dep}} = 853$  K had a columnar

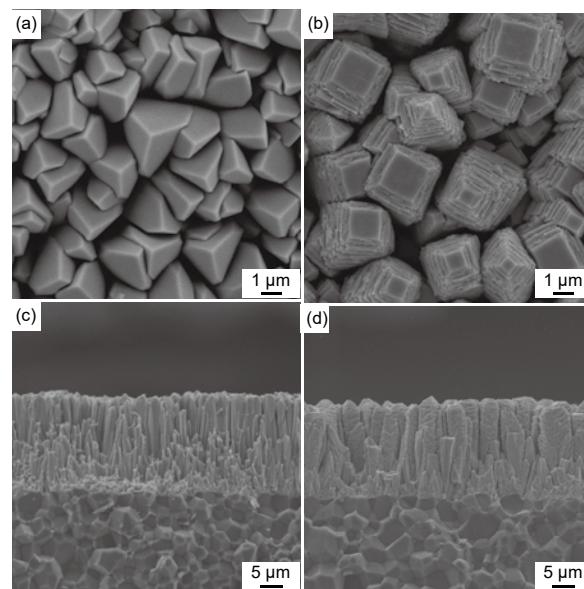


Fig. 1 SEM images of NaTaO<sub>3</sub> films prepared on polycrystalline AlN substrates at  $T_{\text{dep}} = 793$  K (a and c) and 853 K (b and d).

cross-section with a plate-like surface. The photocatalytic hydrogen evolution rate of (001)-NaTaO<sub>3</sub> film reached 5672 mol g<sup>-1</sup> h<sup>-1</sup>, which is 6.4 times higher than that of the (112)-oriented NaTaO<sub>3</sub> film and 3 times higher than that of the films prepared through wet-chemical routes because of the terraced step structure of the (001)-oriented NaTaO<sub>3</sub> film. The solar to hydrogen conversion efficiency of the (001) NaTaO<sub>3</sub> film was 1.93%. Highly (121)- and (*h*21)-oriented SrZrO<sub>3</sub> films were prepared by laser CVD. The hydrogen evolution rate of the SrZrO<sub>3</sub> film prepared by laser CVD reached 960 mol g<sup>-1</sup> h<sup>-1</sup>, which is 20 times higher than that of the film prepared by the solid-state method [2].

### References

- [1] A. M. Huerta-Flores, J. Chen, A. Ito, L. M. Torres-Martínez, E. Moctezuma, and T. Goto, *Mater. Lett.* **184**, 257 (2016).
- [2] A. M. Huerta-Flores, J. Chen, L. M. Torres-Martínez, A. Ito, E. Moctezuma, and T. Goto, *Fuel* **197**, 174 (2017).

Keywords: photocatalytic, chemical vapor deposition (CVD), hydrogen evolution  
Takashi Goto (Multi-Functional Materials Science Division)  
E-mail: goto@imr.tohoku.ac.jp  
URL: <http://www.goto.imr.tohoku.ac.jp/>

## *Electronic Materials*

IMR KINKEN Research Highlights 2018



## Toward Rare-Earth Spintronics

Spintronics studies the flow and conversion of the charge and spin of electrons. Rare earths are heavy atoms characterized by a large spin–orbit interaction that can strongly lock the charge and spin degrees of freedom. This phenomenon allows the manipulation of rare-earth magnetic moments by electric field gradients, which occur naturally at the interfaces of gated *magnetic-insulator–nonmagnetic-metal* heterostructures. A time-dependent voltage can induce, for example, magnetization reversal and ferromagnetic resonance.

The exponential growth of computational capacity yields smaller and denser electric circuits, in which energy dissipation becomes increasingly important. To continue developing more powerful and efficient systems, we need to envision new mechanisms to transmit, read, and write information with lower energy losses. The science and technology called *spintronics* is pushing these aims by focusing on the coupling, flow, and conversion of the charge and spin of electrons. A promising research direction is devoted to the voltage-induced magnetic dynamics discovered in magnetic semiconductors [1] and transition metals [2]. We propose to investigate spintronic effects using heavier atoms, such as *rare earths* or *lanthanides*, which have an extra degree of freedom, namely orbital momentum, even in the solid state. The orbital momentum of rare earths is generated by the net rotation of their inner (*4f*) electrons and couples to the total atomic spin by the strong spin–orbit interaction. Except when empty, full, or half-filled, *4f* shells form an asymmetric charge cloud such as prolate and oblate ellipsoids oriented along the (principal) symmetry axis and the electron spin (see Fig. 1). Gadolinium is the exception, as it is spherical with zero orbital momentum. Because an electric quadrupole can be manipulated by electric fields with large gradients, the magnetic properties that encode the information in computers can be controlled by pure electric fields as well.

Proceeding from these insights, we theoretically analyzed heterostructures containing rare-earth atoms, such as dysprosium and holmium, with an emphasis on the interface of magnetic insulators and nonmagnetic metals, such as copper [3]. An electric field applied in the device cannot penetrate in the metal, which implies that the interface atoms are subject to a nonuniform field that can re-orient a charge quadrupole. This, via the spin–orbit-induced spin–charge locking, generates a torque on the magnetization. We formulate the coupling between the magnetic moment and the applied voltage as the electrostatic energy of charged ellipsoids (the *4f*-sub shells), oriented along the magnetization. Our estimates of the coupling strength find a superior efficiency compared to the known values



Fig. 1 (a) The magnetic subshell of rare earths is elongated (or compressed) along the direction of the orbital momentum  $L$ , which is locked to the spin  $S$ . Their dynamics are therefore rigidly coupled. The curved arrow illustrates the orbital motion of the *4f* electrons.

for transition-metal-based devices [1,2]. Interface moments are embedded into the magnetization by strong exchange interactions, such that the interface torque acts on the total magnetic order. When the voltage is time-dependent, a plethora of dynamical responses mediated by interface rare earths, such as ferromagnetic and parametric resonances, and fast precessional magnetization switching, can be generated.

Large deposits of rare earths have been found in the Japan Exclusive Economic Zone [4], which represents a unique opportunity for the development of many rare-earth-based devices and strong permanent magnets. We hope that our findings invigorate the research for new spintronic effects based on the unique properties of rare-earth-based materials.

### References

- [1] D. Chiba, M. Sawicki, Y. Nishitani, Y. Nakatani, F. Matsukura, and H. Ohno, *Nature* **455**, 515 (2008).
- [2] Y. Shiota, T. Maruyama, T. Nozaki, T. Shinjo, M. Shiraishi, and Y. Suzuki, *Appl. Phys. Express* **2**, 063001 (2008).
- [3] A. O. Leon, A. B. Cahaya, and G. E. W. Bauer, *Phys. Rev. Lett.* **120**, 02720 (2018).
- [4] Y. Kato, K. Fujinaga, K. Nakamura, Y. Takaya, K. Kitamura, J. Ohta, R. Toda, T. Nakashima, and H. Iwamori, *Nat. Geosci.* **4**, 535 (2011).

Keywords: rare earths, spintronics, voltage  
 Alejandro León (Theory of Solid State Physics Division)  
 E-mail: aoleon@imr.tohoku.ac.jp  
 URL: <http://www.bauer-lab.imr.tohoku.ac.jp/>

## Investigating Successive Phase Transition in LiNiPO<sub>4</sub> by Pulsed-High-Magnetic-Field Neutron Diffraction

Successive magnetic-field-induced phase transition of multiferroic compound LiNiPO<sub>4</sub> has been studied by neutron diffraction up to 30 T in pulsed magnetic fields. Alternations of commensurate and incommensurate magnetic structures are observed in accordance with the appearances of polarizations. Of particular interest is that the polarization appears only in commensurate magnetic phases. Such behavior is significantly different from conventional multiferric compounds originated from noncollinear magnetic structures. This shows that a new type of spin–lattice coupling is responsible for multiferroicity in LiNiPO<sub>4</sub>.

LiNiPO<sub>4</sub> has been known as one of the important battery-related materials. Moreover, it shows interesting properties in the magnetic and dielectric behaviors in high magnetic fields, as shown in Fig. 1(a). The magnetization curve shows several metamagnetic anomalies followed by states with nearly flat magnetization. The small fraction of the magnetization to the saturation value suggests the existence of magnetic phases with a long period modulation. When the dielectric constant is measured, it is found that some of the phases are ferroelectric. The central question arising from these behaviors is: What is the magnetic structure of each phase and what is the origin of the successive phase transition?

To determine the magnetic structures in magnetic fields up to 30 T, we have combined a pulsed magnetic field with white pulsed neutron. The experiment was performed at the SEQUIA spectrometer in SNS, USA [1]. With the white neutron beam, we can obtain the Laue diffraction in high magnetic fields. Figure 1(b) shows the intensity map along the b-axis, which is indexed by K. The thin lines are the magnetic field traces as functions of K. Note that the wavevector K or the wavelength of the neutron is related to the time axis of a pulsed magnetic field through the time-of-flight spectrum of the white neutron. To scan a particular magnetic wavevector at a particular magnetic field intensity, the timing between the pulsed magnetic field and the pulsed neutron is adjusted. We found a complex field variation of magnetic wavevectors, as shown in the graph.

Above 12 T,  $K = 0.8$  appears and it disappears at approximately 19 T. The  $K = 1.2$  peak is observed between 16 T and 19 T. There is also intensity at  $K \sim 1$  between 17 and 22 T. Above 22 T, we found a peak at  $K = 1.33$ . More precisely,  $K = 1.2$  is commensurate and others are incommensurate. Such a complex magnetic field variation of magnetic wave the

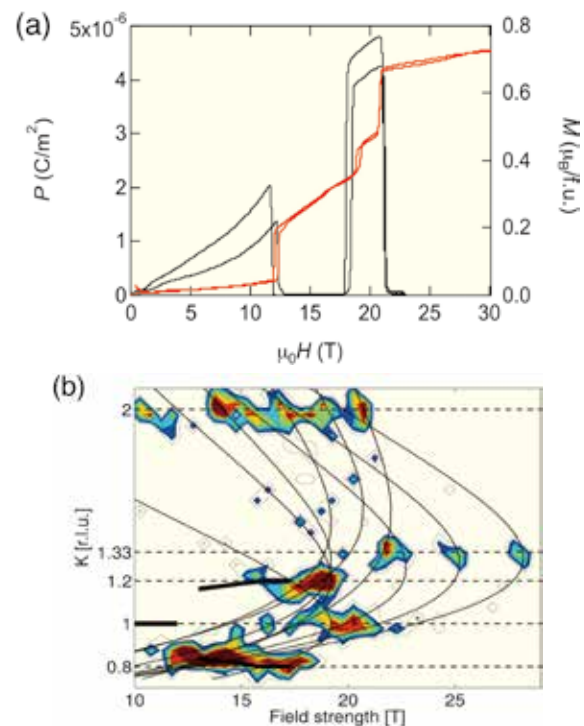


Fig. 1(a) Magnetization curve and the field dependence of the electric polarization. (b) The intensity map of neutron scattering along the  $b^*$ -axis.

neutron Laue method in the pulsed magnetic vector can be determined only with white neutron Laue diffraction in pulsed magnetic fields. The present result shows that the interplay among the competing exchange couplings and the magnetic-field-dependent anisotropy of Ni ions are responsible for the successive phase transition. The contribution of the field-dependent single ion anisotropy may bring a new mechanism for multiferroics.

### References

- [1] R. Toft-Petersen, E. Fogh, T. Kihara, J. Jensen, K. Fritsch, J. Lee, G. E. Granroth, M. B. Stone, D. Vaknin, H. Nojiri, and N. B. Christensen, *Phys. Rev. B* **95**, 064221 (2017).

Keywords: multi-ferroics, neutron diffraction, high magnetic field  
 Hiroyuki Nojiri (Magnetism Division)  
 E-mail: nojiri@imr.tohoku.ac.jp  
 URL: <http://www.hfpm.imr.tohoku.ac.jp/>

## Reconstruction of Spin-Wave Dispersion by Light

We have developed a new method, named spin-wave tomography, to characterize the propagation dynamics of spin waves within the long-wavelength regime, which has been difficult with the conventional methods of spin-wave spectroscopy, with a table-top all-optical method.

The wave motion of atomic spins in a magnet serves as an elementary excitation, a so-called spin wave. To know the properties of the spin wave, one should measure how its frequency changes with its wavenumber vector. This relation is called the dispersion relation, which represents essential information of spin waves. Spin waves whose dispersions are dominated by a dipole–dipole coupling are called pure-magnetostatic waves. These are characterized by anisotropic dispersion relations, representing the anisotropic nature of the dipole–dipole coupling. Although magnetostatic waves have attracted much attention for the application in spintronic and magnonic devices, the observation of dispersion relations of pure-magnetostatic waves has been a challenge. Recently, we developed a new system for the direct observation of the dispersion relation of pure-magnetostatic waves by a table-top all-optical spectroscopic method, which we named spin-wave tomography [1]. Spin waves are excited by the illumination of an ultrashort light pulse focused on the surface of a magnet. When the duration of the pulse and the excitation area are infinitesimally small, the pulse includes all temporal and spatial wave components according to the Fourier theorem. Then, spin waves of all frequency and wavenumber vector can be created and propagate from the excitation point. The created spin waves are detected with a time-resolved magneto–optical imaging system [2]. By Fourier transformation of the observed spin waves with respect to time and spatial coordinates, we obtain the power spectra of the spin waves as a function of frequency and wavenumber vector. By the spectra, the dispersion relation of the spin waves in the pure-magnetostatic region is determined as clearly demonstrated in Fig. 1. This is the basic concept of spin-wave tomography [1]. Afterwards, we used this method to investigate the excitation and the propagation dynamics of optically-excited magnetoelastic waves, which are the hybridized modes of elastic waves and spin waves [3]. Moreover, we developed an advanced procedure of spin-wave tomography, which gives

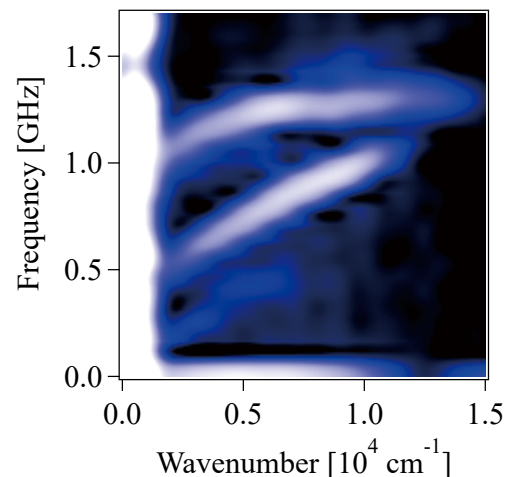


Fig. 1 Dispersion relation of spin waves observed by spin-wave tomography

the phase information of spin waves, and named it phase-resolved spin-wave tomography [4]. The phase-resolved spin-wave tomography was then used to investigate the phase of magnetoelastic waves [5].

### References

- [1] Y. Hashimoto, S. Daimon, R. Iguchi, Y. Oikawa, K. Shen, K. Sato, D. Bossini, Y. Tabuchi, T. Satoh, B. Hillebrands, G. E. W. Bauer, T. H. Johansen, A. Kirilyuk, T. Rasing, and E. Saitoh, *Nat. Commun.* **8**, 15859 (2017).
- [2] Y. Hashimoto, A. R. Khorsand, M. Savoini, B. Koene, D. Bossini, A. Tsukamoto, A. Itoh, Y. Ohtsuka, K. Aoshima, A. V. Kimel, A. Kirilyuk, and T. Rasing, *Rev. Sci. Instrum.* **85**, 063702 (2014).
- [3] Y. Hashimoto, D. Bossini, T. H. Johansen, E. Saitoh, A. Kirilyuk, and T. Rasing, *Phys. Rev. B* **97**, 140404 (2018).
- [4] Y. Hashimoto, T. H. Johansen, and E. Saitoh, *App. Phys. Lett.* **112**, 072410 (2018).
- [5] Y. Hashimoto, T. H. Johansen, and E. Saitoh, *Appl. Phys. Lett.* **112**, 232403 (2018).

Keywords: spin wave, spectroscopy, magnetism

Yusuke Hashimoto<sup>1</sup> and Eiji Saitoh<sup>1,2,3</sup> (<sup>1</sup>AIMR, Tohoku Univ., <sup>2</sup>Surface and Interface Research Division, IMR, <sup>3</sup>JAEA)

E-mail: yusuke.hashimoto.b8@tohoku.ac.jp

URL: <http://saitoh.imr.tohoku.ac.jp/>

## Instant lithography by Water Rinse

Modern electronics is based on various types of nanometer-scale devices fabricated by advanced microfabrication processes. If new materials discovered in laboratories are successfully incorporated into nanodevices, we will utilize new functionalities of electronic devices. The microfabrication of complex materials, however, is not straightforward because process damage usually causes a serious deterioration of the physical properties of the materials. Developing a device process for each new material requires optimization of the process parameters, which often takes much time for a continuous trial-and-error process. Recently, we have developed a versatile microfabrication process using a water-soluble template layer, by which we can pattern an arbitrary material into a desired shape by rinsing in water.

New materials have been continuously discovered in the material science research field, some of which possess characteristic physical properties such as magnetism, ferroelectricity, and superconductivity. Making a functional device out of the discovered new materials is the next step toward their application. Material scientists have expended much effort to develop superior or completely new functionalities for electronic devices by utilizing a variety of emerging materials.

To develop an electronic device out of a new material, we need to pattern the material into a small structure, often on the micrometer or even nanometer scale. However, the physical properties of new materials are often affected by the formation of defects and/or distortions during the device fabrication process. In this study, we developed a versatile damage-free patterning process using a water-soluble template layer, displayed in Fig. 1(a) [1]. First, the  $\text{LaAlO}_3/\text{BaO}_x$  templates (blue layer) are prepared on oxide substrates by room-temperature pulsed laser deposition and a standard photolithography process. Second, the target thin films (red layer) are grown at high temperature. Because of the high melting points of  $\text{LaAlO}_3/\text{BaO}_x$ , the device structure of the template layer can be maintained even in rather extreme conditions, such as several hundred degrees Celsius under high oxygen pressure. Then, the sample is rinsed in water using ultrasonic cleaning. As  $\text{BaO}_x$  has high water solubility, the  $\text{LaAlO}_3/\text{BaO}_x$  layer is removed together with the unnecessary part of the target films. By applying this method, we can pattern arbitrary materials into small structures. Different from the conventional process, severe chemical treatment or plasma treatment are not necessary. We applied the  $\text{LaAlO}_3/\text{BaO}_x$  process to an iron-based superconductor FeSe (Fig. 1(b)) to fabricate micron-scale Hall-bar devices.

The FeSe Hall-bar microdevices exhibit identical

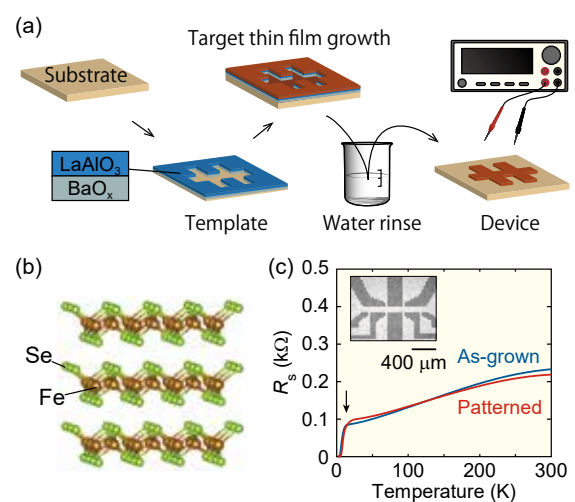


Fig. 1 (a) Process scheme using a  $\text{LaAlO}_3/\text{BaO}_x$  water-soluble template. (b) Crystal structure of FeSe. (c) Temperature dependence of sheet resistance for the patterned (red) and pristine (blue) FeSe films. Inset: optical image of the FeSe Hall-bar.

transport properties with sharp superconducting transition (black arrow) to those of the pristine films (Fig. 1(c)), indicating essentially no damage during the process. We have also succeeded in patterning a representative oxide magnet  $\text{SrRuO}_3$ , which demonstrates the versatility of the patterning process. We are now exploiting the  $\text{LaAlO}_3/\text{BaO}_x$  process to fabricate various types of devices. Recently, we have discovered an anomalous behavior of critical current density in ultrathin FeSe devices [2]. The water-based soft-lithography process would expand the range of application of emerging materials in electronic devices.

### References

- [1] T. Harada and A. Tsukazaki, *AIP Adv.* **7**, 085011 (2017).
- [2] T. Harada, J. Shiogai, T. Miyakawa, T. Nojima, and A. Tsukazaki, *Supercond. Sci. Technol.* **31**, 055003 (2018).

Keywords: devices, thin films, oxide

Takayuki Harada (Low Temperature Physics Division)

E-mail: t.harada@imr.tohoku.ac.jp

URL: <http://mu.imr.tohoku.ac.jp/>

## Understanding How Itinerant Electrons in Solids Turn to Glass

New insights into the behavior of itinerant electrons in an organic crystal as liquids transform to the charge-glass state are deepening our understanding of the universal nature of the liquid-to-glass transition.

Glassy materials are ubiquitous in nature. The history of glassmaking traces back thousands of years and sophisticated glass-forming technology has been utilized by mankind for centuries. Yet, the fundamental understanding of glassy dynamics remains one of the most important unresolved problems in both physics and materials science. We focus on a unique glassy state of electrons in solids realized in an organic molecular conductor [1], schematically shown in Fig. 1, where the lack of periodicity of the strongly correlated electrons on the triangular lattice is caused by geometrical frustration and strong quantum effects.

The quasi-two-dimensional organic compound  $\theta_m$ -(BEDT-TTF) $_2$ TlZn(SCN) $_4$  undergoes a charge ordering (CO) transition at  $T_m \sim 170$  K owing to strong electron correlations, where the charge carriers on the BEDT-TTF molecules are localized periodically. Such a CO state can be regarded as a “charge-crystal” state. In contrast, above the CO transition temperature, the charge is distributed uniformly in space, which is referred to as a “charge-liquid” state. When the sample is cooled faster than a critical cooling rate ( $\sim 50$  K/min), charge crystallization is kinetically avoided, leading to a “charge-glass” state in which the charges are randomly quenched.

We quantitatively evaluated the CO volume fraction from the time evolution of the resistivity during the charge crystallization process from the super-cooled charge-liquid or charge-glass state. Figure 2 displays a contour map of the CO fraction plotted in the time–temperature plane, which is a so-called time–temperature–transformation (TTT) diagram. The relaxation time becomes faster with decreasing temperature, and then slower below  $\sim 160$  K, which is referred to as the “nose temperature”; this characteristic temperature dependence of the relaxation time can be explained by the theory of nucleation and growth at a first-order liquid–crystal phase transition. Our observation demonstrates that the crystallization process of electrons in solids can be described by the nucleation and growth process of a liquid, as observed in conventional glass-forming liquids.

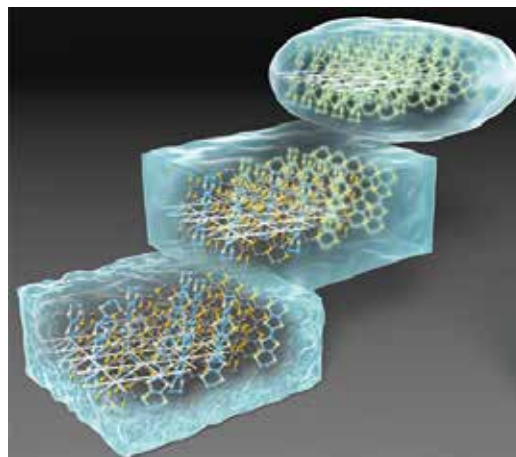


Fig. 1 Electrons transition from a liquid state (top) to a glassy state (bottom) upon cooling.

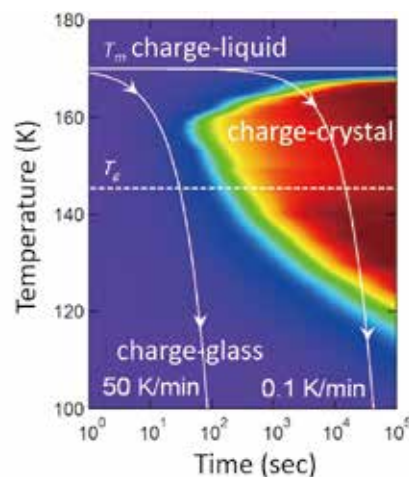


Fig. 2 TTT diagram of the organic compound  $\theta_m$ -(BEDT-TTF) $_2$ TlZn(SCN) $_4$  derived from the time evolution of the resistivity reflecting the CO volume fraction.

Surprising similarities between our system and conventional glass formers highlight the universal nature of the liquid–glass transition.

### References

- [1] S. Sasaki, K. Hashimoto, R. Kobayashi, K. Itoh, S. Iguchi, Y. Nishio, Y. Ikemoto, T. Moriwaki, N. Yoneyama, M. Watanabe, A. Ueda, H. Mori, K. Kobayashi, R. Kumai, Y. Murakami, J. Müller, and T. Sasaki, *Science* **357**, 1381 (2017).

Keywords: glass, organic, metal–insulator transition

Kenichiro Hashimoto (Low Temperature Condensed State Physics Division)

E-mail: hashimoto@imr.tohoku.ac.jp

URL: <http://cond-phys.imr.tohoku.ac.jp/>

# Charge Density Wave Order Insensitive to Superconductivity in Electron-Doped High- $T_c$ Superconductor

The interplay between charge density wave (CDW) and superconductivity have attracted much attention in the research of high- $T_c$  superconductivity. We have revealed that in an electron-doped system, the CDW is insensitive to superconductivity, suggesting a different nature from the CDW order in hole-doped systems.

The high-temperature superconductivity in copper oxides appears with carrier doping into an antiferromagnetic Mott insulator (Fig. (a)). There are two types of the superconductors: hole-doped and electron-doped systems, where the carrier charge is positive and negative, respectively. The electron–hole asymmetry is one of most important issues for the unified understanding of high- $T_c$  superconductivity. Recent developments in synchrotron X-ray scattering measurements have been revealing the existence of charge density wave (CDW) order [1,2]. The detailed nature of the CDW is still under investigation, particularly in electron-doped systems, whereas in the hole-doped systems, it has been established that the CDW formation is due to an instability of the electronic structure at the Fermi surface and competes with the superconductivity.

Here, we first performed Cu  $L_{3}$ -edge resonant soft X-ray scattering (RSXS) measurements for representative electron-doped high- $T_c$  superconductors  $\text{Nd}_{2-x}\text{Ce}_x\text{CuO}_4$  (NCCO) [3]. Annealed NCCO shows superconductivity, whereas as-grown (non-annealed) NCCO does not. Therefore, NCCO is suitable for investigating the relation between superconductivity and CDW. Figure (c) shows RSXS scans along the  $h$  direction in  $q = (h, 0)$  for superconducting annealed NCCO. A clear peak is observed at  $h = 0.26$ , which is indicative of the putative CDW order in electron-doped systems [2]. A new finding is that the peak is also observed in nonsuperconducting as-grown NCCO at the same position. Detailed studies of temperature, energy, and angle dependencies further confirm the insensitive nature to superconductivity.

Moreover, to investigate the origin of the peak, we have carried out angle-resolved photoemission spectroscopy (ARPES) on the same crystal as used in RSXS. Figure (e) shows an ARPES spectrum along the  $k_y$  direction at  $(\pi, 0)$  of the Fermi surface. The peaks are positioned definitely off outwardly from  $k_y = 0.26$ , corresponding to the wavevector in the RSXS results. Furthermore, the peak position depends on the annealing condition. These ARPES results suggest that the instability of the electronic structure cannot account for the peak observed in RSXS. These combined results of RSXS and ARPES call into question the universality of the

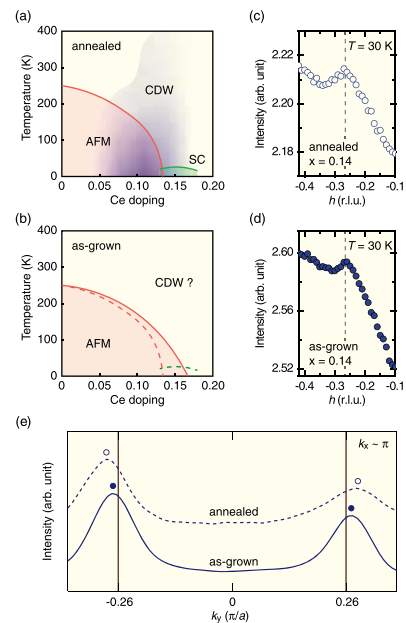


Fig. Phase diagram of (a) annealed and (b) as-grown NCCO as a function of Ce doping. Antiferromagnetic order (AFM) disappears with Ce doping and the superconductivity (SC) and charge density wave (CDW) appear in the annealed NCCO. (c)(d) RSXS intensities for annealed and as-grown NCCO, respectively. The peak indicated by the dashed line demonstrates the existence of CDW. (e) ARPES spectra along  $k_y$  at the Fermi surface. The peak positions are definitely off outwardly from  $k_y = 0.26$ , which is the RSXS peak position.

CDW in high- $T_c$  superconductivity [3].

## References

- [1] G. Ghiringhelli, M. Le Tacon, M. Minola, S. Blanco-Canosa, C. Mazzoli, N. B. Brookes, G. M. De Luca, A. Frano, D. G. Hawthorn, F. He, T. Loew, M. Moretti Sala, D. C. Peets, M. Salluzzo, E. Schierle, R. Sutarto, G. a. Sawatzky, E. Weschke, B. Keimer, and L. Braicovich, *Science* **337**, 821 (2012).
- [2] E. H. da Silva Neto, R. Comin, F. He, R. Sutarto, Y. Jiang, R. L. Greene, G. A. Sawatzky, and A. Damascelli, *Science* **347**, 282 (2015).
- [3] H. Jang, S. Asano, M. Fujita, M. Hashimoto, D. H. Lu, C. A. Burns, C. C. Kao, and J. S. Lee, *Phys. Rev. X* **7**, 2 (2017).

Keywords: superconducting, X-ray scattering, electronic structure  
Masaki Fujita (Quantum Beam Materials Physics Division)  
E-mail: qblab@imr.tohoku.ac.jp  
URL: <http://qblab.imr.tohoku.ac.jp>

## Magneto–Ionic Control in a Honeycomb-Layer Metal–Organic Framework Using a Li-Ion Battery System

Magnetic phase stability was modulated by controlling the radical spin generation/annihilation via electron doping to a metal–organic framework using a Li-ion battery system. The electron (spin)-inserted state generated in the discharge process had a higher magnetic phase transition temperature ( $T_{c2} = 33$  K) than that of the pristine form ( $T_{c1} < 10$  K), which demonstrated reversible phase switching between para- and ferri-magnetic phases in the range of  $T_{c1} < T < T_{c2}$  by repeating charge/discharge treatments.

In recent years, there has been growing interest in electrical magnetism control based on redox-reactions accompanied by ion transportation; i.e., magneto–ionic control [1–5]. Magneto–ionic control achieves an electrochemical equilibrium in a material, such that the electrically modulated magnetic phase should be nonvolatile. This situation inspires possible applications of functional devices, such as magnetoelectric memory with a low power consumption.

The Li<sup>+</sup>-ion battery (LIB) is a representative ion-transporting redox system, in which Li<sup>+</sup> ions and electrons simultaneously migrate between two electrodes. Hence, we could control the electron density of the electrode material; e.g., the cathode is filled with electrons (and Li<sup>+</sup> ions) in the discharge process. Using this concept, we have attempted to control the radical spin generation/annihilation in the bridging ligands of metal–organic frameworks (MOFs) through discharge/charge cycles of a LIB system [3–5].

As a MOF-cathode, we have focused on a well-known honeycomb-layer ferrimagnet; (NBu<sub>4</sub>) [Mn<sup>II</sup>Cr<sup>III</sup>(Cl<sub>2</sub>An)<sub>3</sub>] (NBu<sub>4</sub><sup>+</sup> = tetra(*n*-butyl)ammonium ion, Cl<sub>2</sub>An<sup>2-</sup> = chloranilate), which underwent ferrimagnetic ordering at  $T_{c1} < 10$  K because of the superexchange interaction between Mn<sup>2+</sup> ( $S = 5/2$ ) and Cr<sup>3+</sup> ( $S = 3/2$ ) via the nonmagnetic bridging ligand Cl<sub>2</sub>An<sup>2-</sup> ( $S = 0$ ). Because Cl<sub>2</sub>An<sup>2-</sup> experiences a reduction to a radical state Cl<sub>2</sub>An<sup>3•-</sup> ( $S = 1/2$ ), this material was used as a cathode, which could control the magnetic phase stability tuned by a newly produced exchange pathway associated with selective electron-filling at the bridging ligand based on LIB.

The ferrimagnetic phase was indeed stabilized in the discharged state with an increase in transition temperature ( $T_{c2} \sim 33$  K). However, in the charged state,  $T_c$  went back to the initial  $T_{c1}$  state (Fig. 1). Reflecting the different states between the discharged and charged states, the reversible

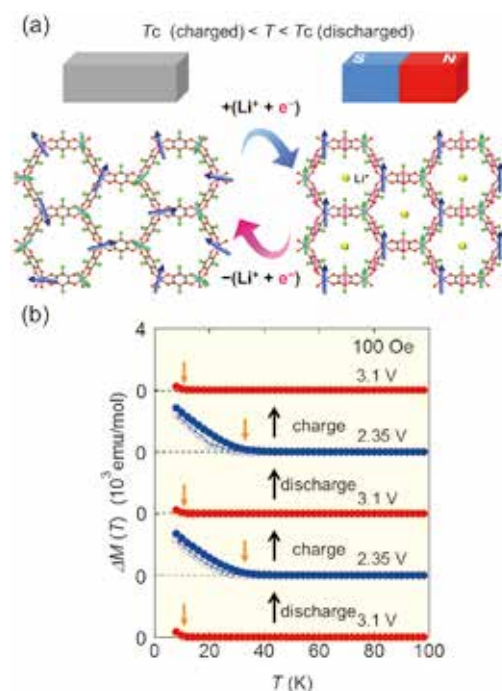


Fig. 1 (a) Schematic figure of magnetism control in MOF by LIB system. (b) Reversible control of magnetic phase stability by *in situ* LIB cell.

magnetic phase switching between the paramagnetic and ferrimagnetic states was demonstrated in the temperature range of  $T_{c1} < T < T_{c2}$  [5].

These results could pave the way to the emerging field of magneto–ionics.

### References

- [1] N. Lu *et al.* Nature. **546**, 124 (2017).
- [2] U. Bauer *et al.* Nat. Mat. **14**, 174 (2015).
- [3] K. Taniguchi, K. Narushima, J. Mahin, W. Kosaka, and H. Miyasaka, Angew. Chem. Int. Ed. **55**, 5238 (2016).
- [4] K. Taniguchi, K. Narushima, H. Sagayama, W. Kosaka, N. Shito, and H. Miyasaka, Adv. Funct. Mater. **27**, 1604990 (2017).
- [5] K. Taniguchi, J. Chen, Y. Sekine, and H. Miyasaka, Chem. Mater. **29**, 10053 (2017).

Keywords: magnetic properties, molecular devices, electron doping

Kouji Taniguchi and Hitoshi Miyasaka (Solid-State Metal-Complex Chemistry Division)

E-mail: taniguchi@imr.tohoku.ac.jp (K. T.), miyasaka@imr.tohoku.ac.jp (H. M.)

URL: <http://www.miyasaka-lab.imr.tohoku.ac.jp/>

# Monolayer-Controlled Co | Ni Epitaxial Superlattices with High Magnetic Anisotropy and Low Magnetic Damping

High magnetic anisotropy energy ( $K$ ) and low magnetic damping constant ( $\alpha$ ) are key properties for materials of future spintronic devices. Here, we show that monolayer-controlled Co | Ni epitaxial superlattices simultaneously exhibit higher  $K$  and lower  $\alpha$  than conventional textured superlattices. Our systematic investigation revealed the origin of magnetic anisotropy and magnetic damping for Co | Ni superlattices.

Magnetic materials with high magnetic anisotropy ( $K$ ) and low magnetic damping ( $\alpha$ ) have attracted much attention, because both are key properties to realize a high storage density and low power consumption for operation in spintronic devices, and a perpendicularly magnetized Co | Ni multilayer is one of the promising candidates [1]. The main purpose of this study is to develop Co | Ni epitaxial superlattices with simultaneously high  $K$  and low  $\alpha$  by utilizing a monolayer (ML)-controlled deposition technique [2].

A molecular beam epitaxy (MBE) system was employed to grow the ML-controlled Co | Ni multilayers. The epitaxial Co | Ni superlattices were grown on an  $\text{Al}_2\text{O}_3$  (11-20) single-crystal substrate with V | Au buffer layers and a Au capping layer. The number of MLs for each Ni layer ( $x$ ) was varied in the range from 1 to 4 and the Co layer thickness was fixed at 1 ML, where 1 ML corresponded to 0.2 nm for both Co and Ni layers. For comparison, textured Co | Ni were prepared on a thermally oxidized Si substrate.

Figure 1(a) displays a two-dimensional (2D) diffraction intensity mapping for  $x = 1$  grown on the  $\text{Al}_2\text{O}_3$  (11-20) single-crystal substrate. We also constructed the cross-section of reciprocal space for the CoNi 200 and the Au 200 diffractions (Fig. 1(b)). The six-fold rotational symmetries for both the CoNi 200 and the Au 200 indicate that the Co | Ni multilayer was epitaxially grown on the  $\text{Al}_2\text{O}_3$  (11-20) single-crystal substrate with the Au / V buffers.

The effective  $K$  ( $K_{\text{eff}}$ ) and effective minimum  $\alpha$  ( $\alpha_{\text{eff,min}}$ ) as functions of  $x$  are summarized in Figs. 2(a) and 2(b), respectively. For each  $x$ , the epitaxial Co | Ni shows higher  $K_{\text{eff}}$  and lower  $\alpha_{\text{eff,min}}$  than those for the textured one, resulting in the perpendicular magnetization with low  $\alpha$ , even for the 1 ML-Ni | 1 ML-Co. The first-principles calculation indicated that the Ni atoms largely contributed to  $K$  for the Co | Ni multilayers. We also found that  $\alpha$  was related to the density of states at the Fermi energy. The present results suggest that the epitaxial Co | Ni

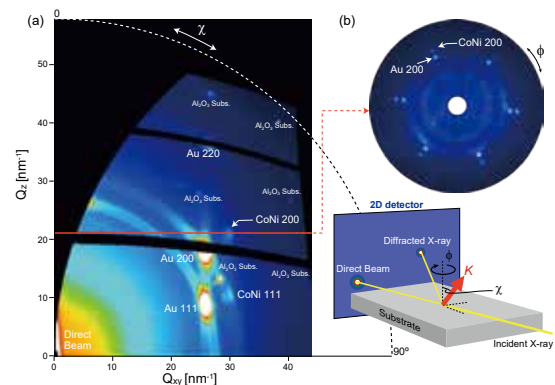


Fig. 1 (a) Two-dimensional (2D) diffraction intensity mapping for  $x = 1$  grown on the  $\text{Al}_2\text{O}_3$  (11-20) single crystal substrate. (b) Cross-section of reciprocal space for the CoNi 200 and the Au 200 diffractions.

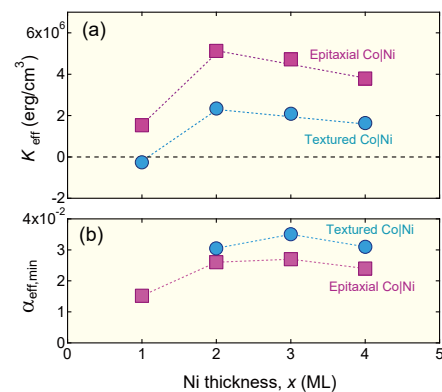


Fig. 2 (a) Effective  $K$  ( $K_{\text{eff}}$ ) and (b) effective minimum  $\alpha$  ( $\alpha_{\text{eff,min}}$ ) as functions of  $x$  for the epitaxial Co | Ni and the textured Co | Ni.

superlattice is a promising material to simultaneously achieve high  $K_u$  and low  $\alpha$ .

## References

- [1] A. D. Kent, and D. C. Worledge, Nature Nanotech. **10**, 187 (2015).
- [2] T. Seki, J. Shimada, S. Iihama, M. Tsujikawa, T. Koganezawa, A. Shioda, T. Tashiro, W. Zhou, S. Mizukami, M. Shirai, and K. Takahashi, J. Phys. Soc. Jpn. **86**, 074710 (2017).

Keywords: magnetic properties, molecular beam epitaxy (MBE), spin dynamics  
 Koki Takahashi (Magnetic Materials Division)  
 E-mail: koki@imr.tohoku.ac.jp  
<http://magmatelab.imr.tohoku.ac.jp/>

## Mechanism of Two-Dimensional Nucleation of Colloidal Crystals

Understanding the nucleation and growth mechanism of a colloidal crystal is critical for applying it to novel functional devices such as photonic crystals. In-situ observations at single-particle resolution enable us to measure the steady-state homogeneous two-dimensional nucleation rate and the critical size of nuclei, and the relationship between them and particle concentration is found to agree well with the classical nucleation theory. The step free energy deduced from the nucleation theory is found to change according to the strength of attraction between particles.

Because the lattice constant of colloidal crystals is comparable to the wavelength of visible light, they are expected to be applied to novel photonic devices. Particle interactions, such as repulsive, attractive and hard-sphere, are a significant key factor for fabricating these novel nanostructured materials. Attractive interactions have recently been well utilized. The attractive forces can be used to fabricate a variety of structures that are not obtained only by repulsive interactions between particles. However, the growth mechanism of colloidal crystals with attractive interaction has not been clarified. We have investigated two-dimensional (2D) nucleation on the terrace of colloidal crystals, in which added polymers generate a depletion attraction for a balance between colloidal particles [1].

We found that 2D nucleation is the predominant growth mechanism in the system, where 2D islands nucleate repeatedly and spread on the surface (Fig. 1(A)). Particles are brought to the terrace from the solution, diffuse there over a certain length and time, and then return to solution. When a particle on the terrace reaches a step, it is incorporated into the crystal, which advances a step of 2D islands. Some particles occasionally form clusters, and a nucleus is formed when those clusters grow. We recognized a critical size of nucleation, that is, smaller embryos shrink and then disappear, whereas larger embryos keep growing. This nucleation process follows the framework of the classical nucleation theory (CNT).

We introduce the area fraction,  $\phi_{\text{area}}$ , as the surface area concentration of colloidal particles. The relationship between the nucleation rate,  $J$ , and the critical radius,  $r^*$ , versus  $\phi_{\text{area}}$  is investigated. Based on the CNT,  $J$  and  $r^*/a$  are plotted, as in Fig. 1(B) and (C) respectively. The equilibrium volume fraction,  $\phi_{\text{eq}}$ , is measured experimentally as the value of  $\phi_{\text{area}}$  at which the growth rate of the steps of two-dimensional islands is zero. The linear relation between  $\ln J$  and  $1/\ln(\phi_{\text{area}}/\phi_{\text{eq}})$  indicates that the nucleation behavior is the nucleation process of

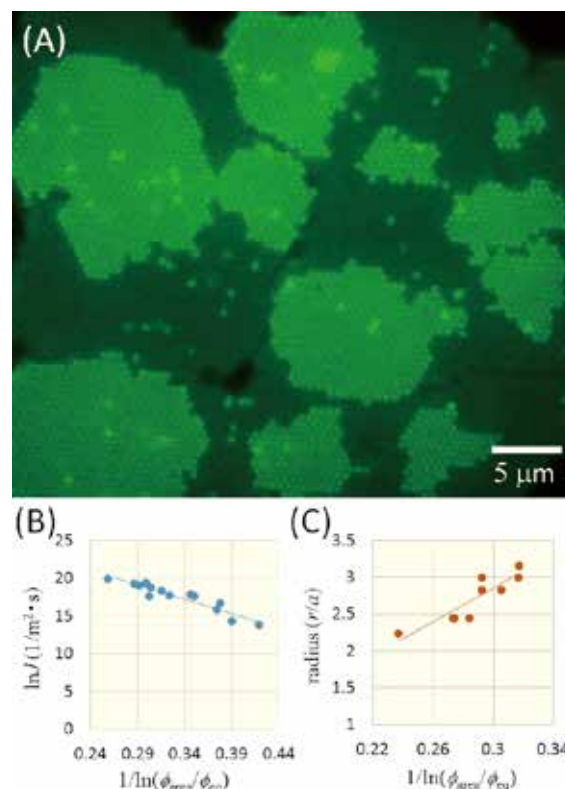


Fig. 1 (A) Nucleation and growth of 2D islands observed with single-particle resolution. (B)  $\ln J$  as a function of  $1/\ln(\phi_{\text{area}}/\phi_{\text{eq}})$ . (C)  $r^*/a$ , as a function of  $1/\ln(\phi_{\text{area}}/\phi_{\text{eq}})$ .

colloidal crystals, which agrees well with the CNT.

We investigated the 2D nucleation of colloidal crystals on a glass slide [2], which also essentially follows the CNT, and the interfacial energy between the substrate and crystal is found to play an important role in the nucleation process.

### References

- [1] J. Nozawa, S. Uda, S. Guo, S. Hu, A. Toyotama, J. Yamanaka, J. Okada, and H. Koizumi, *Langmuir* **33**, 3262 (2017).
- [2] S. Guo, J. Nozawa, S. Hu, H. Koizumi, J. Okada, and S. Uda, *Langmuir* **33**, 10543 (2017).

Keywords: colloid, crystal growth, nucleation & growth  
 Jun Nozawa (Crystal Chemistry Division)  
 E-mail: nozawa@imr.tohoku.ac.jp  
 URL: <http://www.uda-lab.imr.tohoku.ac.jp/index.html>

## Field-Tuned Cooper Pairs in Ferromagnetic Superconductivity

The coexistence of ferromagnetism and superconductivity attracts much attention, because novel quantum phenomena based on the novel superconducting mechanism are expected. The field-reentrant or field-reinforced superconductivity is one of the highlights in unconventional superconductivity. Here, we found that the Cooper pairs in the ferromagnetic superconductor UCoGe become robust with increasing field when the field is applied along the hard-magnetization axis. The enigma of ferromagnetic superconductivity was unveiled by means of low-temperature high-field experiments using high quality single crystals.

Superconductivity and magnetism are antagonistic in the conventional theory of superconductivity. In particular, ferromagnetism is harmful, because the large internal field easily destroys the superconducting Cooper pairs. The discovery of ferromagnetic superconductivity in UGe<sub>2</sub>, URhGe, and UCoGe introduced a new paradigm for unconventional superconductivity. The spin-triplet state with equal spin pairing is naturally expected, because the pair-breaking due to the ferromagnetism does not occur. Furthermore, the spectacular field-reentrant (field-reinforced) superconductivity was discovered in these three compounds. The mechanism for this phenomenon remains unclear.

In order to investigate the field-reinforced superconductivity, we grew high-quality single crystals of UCoGe and performed transport measurements at very low temperature down to 10 mK and at high field up to 15 T, with fine tuning of the field direction [1]. Figure 1 shows the temperature dependence of the upper critical field  $H_{c2}$  for the field along the b-axis in the orthorhombic structure in UCoGe. The  $H_{c2}$  curve shows the so-called S-shape, indicating that superconductivity is abruptly enhanced at high field. As schematically shown in Fig. 1, it is found that the strength of the Cooper pairs, which stabilizes superconductivity, is field-dependent and becomes large at high field. Furthermore, it was also demonstrated that the Ising-type ferromagnetic fluctuations are strongly enhanced for the field along the b-axis. The ferromagnetic fluctuations are very sensitive to the field direction. When the field is applied along the easy magnetization c-axis instead, the ferromagnetic fluctuations are immediately suppressed, leading to a small  $H_{c2}$ . The anisotropic field response is in contrast to the case for the A1-phase of <sup>3</sup>He, where the electrons with only one direction are paired.

This work was done in collaboration with G. Knebel, A. Poursret, B. Wu, G. Bastien, M. Taupin, C.

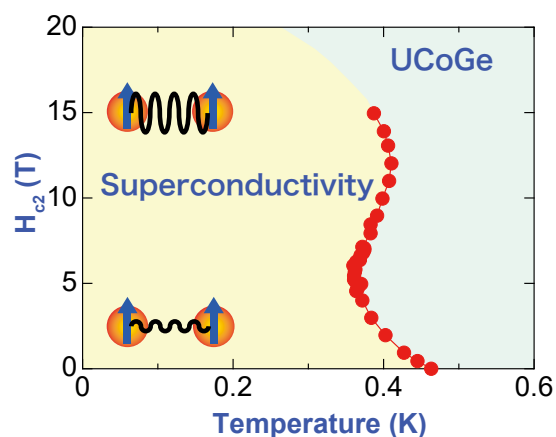


Fig. 1 Temperature dependence of the upper critical field  $H_{c2}$  for  $H // b$ -axis in the ferromagnetic superconductor UCoGe. The strength of superconducting Cooper pairs increases with the field.

Paulsen, L. Howald, J. P. Brison, and J. Flouquet in CEA-Grenoble.

### References

- [1] B. Wu, G. Bastien, M. Taupin, C. Paulsen, L. Howald, D. Aoki, and J. P. Brison, *Nat. Commun.* **8**, 14480 (2017).

Keywords: superconducting, heavy fermion  
Dai Aoki (Actinide Materials Science Division)  
E-mail: aoki@imr.tohoku.ac.jp  
<http://actinide.imr.tohoku.ac.jp/>

## Low-Temperature Deposition of Piezo-Films Using Hydrothermal Method

Flexible piezo-films have been widely investigated in a variety of applications. To fabricate such films, it is essential to deposit piezo-films on organic substrates. Normally, the heatproof temperature of organic substrates is less than 200 °C, whereas most of the deposition methods require temperatures higher than 500 °C to form piezo-films. Therefore, it is difficult to realize flexible piezo-films. In this study, the possibility of low-temperature deposition of piezo-films using a hydrothermal method was investigated.

KNbO<sub>3</sub> films, which is one of the piezo-films with a perovskite structure, were deposited on (100) cSrRuO<sub>3</sub>/(100)SrTiO<sub>3</sub> substrates as well as KNbO<sub>3</sub> powders for 6 h by a hydrothermal method. The raw materials were Nb<sub>2</sub>O<sub>5</sub> powder and KOH solution. These source materials and substrates were sealed in an autoclave, which was set in a thermostat bath maintained at a fixed temperature. After preparation, the KNbO<sub>3</sub> films and powders were ultrasonically washed, and then dried under the deposition temperature in air.

Figure 1 shows XRD  $2\theta$ - $\omega$  profiles of films deposited at various temperatures. All XRD profiles showed only {001}<sub>c</sub> diffraction peaks of the perovskite structure. In addition, these films were epitaxially grown on substrates. Therefore, {001}-oriented epitaxial KNbO<sub>3</sub> films were obtained even at a low temperature of 120 °C. Figure 2 shows XRD  $2\theta$ - $\omega$  profiles of powders prepared simultaneously in the same batch shown in Fig. 1. In the case of 240 °C deposition, only KNbO<sub>3</sub> powder was obtained. However, the diffraction peaks arising from the secondary phase, such as Nb<sub>2</sub>O<sub>5</sub> and K<sub>3</sub>Nb<sub>7</sub>O<sub>19</sub>, were observed with decreasing deposition temperature. This means that it is difficult to obtain KNbO<sub>3</sub> powders at a synthesis temperature lower than 150 °C.

From above results, it is considered that KNbO<sub>3</sub> films can be obtained even at a low temperature of 120 °C, because the SrRuO<sub>3</sub> layer with a perovskite structure accelerated the inhomogeneous nucleation. In fact, the homogeneous nucleation of the perovskite structure has not been achieved at such a low temperature. Therefore, it was found that the design of the surface layer of a substrate is a key to obtaining piezo-films at a low temperature by a hydrothermal method. Using this technique, it is possible to fabricate flexible piezo-films. [1,2]

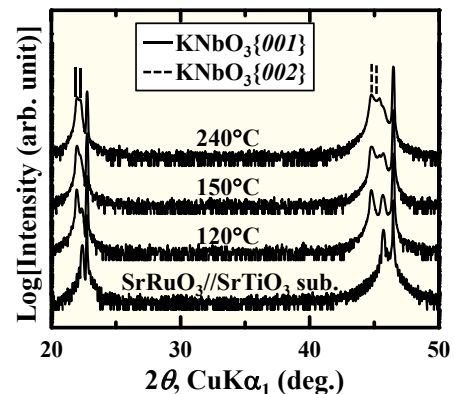


Fig. 1 XRD  $2\theta$ - $\omega$  profiles of films deposited at various temperature.

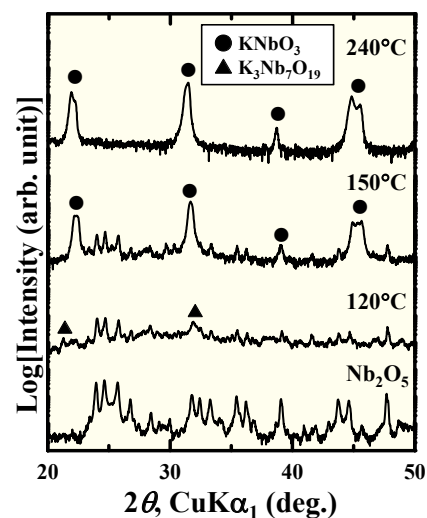


Fig. 2 XRD  $2\theta$ - $\omega$  profiles of powders simultaneously synthesized with KNbO<sub>3</sub> films.

### References

- [1] T. Shiraishi, N. Kaneko, M. Ishikawa, M. Kurosawa, H. Uchida, and H. Funakubo, *Jpn. J. Appl. Phys.* **53**, 09PA10 (2014).
- [2] T. Shiraishi, M. Ishikawa, H. Uchida, T. Kiguchi, M. K. Kurosawa, H. Funakubo, and T. J. Konno, *Jpn. J. Appl. Phys.* **56**, 10PF04 (2017).

Keywords: hydrothermal, piezoelectric, thin films

Takahisa Shiraishi (Materials Science of Non-Stoichiometric Compounds Division)

E-mail: takahisa.shiraishi@imr.tohoku.ac.jp

URL: <http://konno-lab.imr.tohoku.ac.jp/index.html>

## Different Photoisomerization Routes in the Structural Isomers of Cinnamate-Based Sunscreens

The Professional development Consortium for Computational Materials Scientists (PCoMS) supports young researchers in computational materials science to develop their broader view and extensive knowledge of interdisciplinary areas among materials science, condensed matter physics, molecular science, and materials design. Introduced below is a recent study by one of the key members of PCoMS. Prof. Yamazaki and coauthors both theoretically and experimentally found that the photoisomerization pathways of cinnamate-based sunscreens depend on their substitution positions.

Cinnamate derivatives are widely used molecules in nature and industry, as the chromophore of photo-active yellow protein, sunscreens of many plants to protect their DNA, UV absorber of sunscreen cosmetics, etc. Understanding the nonradiative decay (NRD) mechanisms should enable the realization of new effective sunscreens and other photofunctional materials. In this study, we investigated the NRD pathways of jet-cooled *para*-methoxy methylcinnamate (*p*-MMC) and *para*-methoxy ethylcinnamate (*p*-MEC), *ortho*-, *meta*-, and *para*-hydroxy methylcinnamate (*o*-, *m*-, and *p*-HMC, respectively) by picosecond and nanosecond pump-probe spectroscopy, and low-temperature matrix-isolation Fourier Transform Infrared Spectroscopy (FTIR) spectroscopy. The possible NRD pathways were calculated by the single-component artificial force induced reaction (SC-AFIR) method combined with the time-dependent density functional theory.

We found that the all investigated cinnamate-based sunscreens undergo *trans* → *cis* photoisomerization under UV irradiation, but differ in the isomerization pathway. *p*-MMC, *p*-MEC, and *p*-HMC are isomerized via multistep intersystem crossing (ISC) from the bright  $^1\pi\pi^*$  state to the  $^3\pi\pi^*$  state, mostly via stepwise ISC followed by the internal conversion (IC) from  $^1\pi\pi^*$  to the dark  $^1n\pi^*$  state (Fig. 1) [1,2].

However, *m*- and *o*-HMC are directly isomerized by twisting along the C=C double bond to 90° on the  $S_1$  state and subsequent IC to the electronic ground ( $S_0$ ) state (Fig. 2) [2]. These results suggest that controlling the substitution position is essential for designing the cinnamate-based photofunctional materials.

### References

[1] K. Yamazaki, Y. Miyazaki, Y. Harabuchi, T. Taketsugu, S.

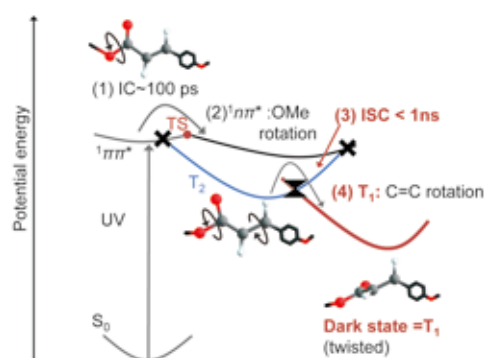


Fig. 1 Multistep intersystem crossing (ISC) pathway of *p*-MMC, which is followed by the internal conversion (IC) from  $^1\pi\pi^*$  to the dark  $^1n\pi^*$  state.

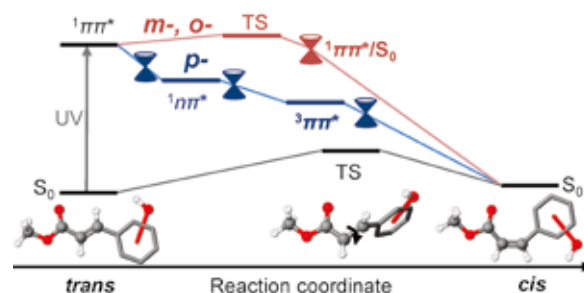


Fig. 2. Schematic of the photo-isomerization pathway of HMC-based sunscreens with different substitution positions [2]. *p*-HMC are isomerized via multistep intersystem crossing (ISC) from the bright  $^1\pi\pi^*$  state to the  $^3\pi\pi^*$  state. In contrast, *m*- and *o*-HMC are directly isomerized by twisting along the C=C double bond to 90° on the  $S_1$  state and subsequent IC to the  $S_0$  state.

Maeda, Y. Inokuchi, S. Kinoshita, M. Sumida, Y. Onitsuka, H. Kohguchi, M. Ehara, and T. Ebata, J. Phys. Chem. Lett. **7**, 4001 (2016).

[2] S. Kinoshita, Y. Miyazaki, M. Sumida, Y. Onitsuka, H. Kohguchi, Y. Inokuchi, N. Akai, T. Shiraogawa, M. Ehara, K. Yamazaki, Y. Harabuchi, S. Maeda, T. Taketsugu, and T. Ebata, Phys. Chem. Chem. Phys., DOI: 10.1039/C8CP00414E (2018) in press (Featured on the back cover).

Keywords: organic, first-principles calculations, electronic structure

Kaoru Yamazaki (Professional development Consortium for Computational Materials Scientists)

E-mail: kaoru.yamazaki@imr.tohoku.ac.jp

Tetsuo Mohri (Project Leader of Professional development Consortium for Computational Materials Scientists)

URL: <http://pcoms.imr.tohoku.ac.jp/index.html>

## *Research Centers*

IMR KINKEN Research Highlights 2018



# Novel STEM Imaging of Dislocation Loops in Steels

International Research Center for Nuclear Materials Science

The size distribution and number density of small dislocation loops are some of the most important structural parameters for characterizing the hardening of steel/metallic alloy. In transmission electron microscopy (TEM), an accurate quantification of such nanoscaled defects heterogeneously dispersing in the matrix has been a significant challenge for over 60 years, because of strong interference artifacts due to the parallel wave of TEM. The convergent electron wave and dedicated scanning system of weak-beam scanning TEM are highlighted as a solution for radiation damage.

To achieve more accurate quantification of lattice defects in steels and metallic alloy samples, an advanced spherical-aberration-corrected transmission electron microscope in the Oarai center was innovatively modified in 2016. The design of a new optics system for the diffraction contrast imaging of dislocation loops was named as weak-beam scanning transmission electron microscopy (WB-STEM). By installing a novel beam selector, Howie's detector, a high-speed CCD camera, and imaging filter in a camera chamber of an aberration-corrected electron microscope, nonlinear contrast imaging consisting of WB-STEM imaging and 3D electron tomography were achieved in addition to conventional elemental analyses, such as STEM-Energy dispersive X-ray spectrometry (EDS) and STEM-electron energy loss spectroscopy (EELS) (Fig. 1(a)).

The capabilities of the WB-STEM were firstly applied to neutron-induced lattice defects in reactor pressure vessel (RPV) steels. Systematic WB-STEM analyses of size distribution and number density of dislocation loops in each RPV steel with neutron fluences of  $1.3 \times 10^{23}$ ,  $3.4 \times 10^{23}$ ,  $8.2 \times 10^{23}$ , and  $1.2 \times 10^{24} \text{ n m}^{-2}$  with a flux of  $1.3 \times 10^{15} \text{ n m}^{-2} \text{ s}^{-1}$  are finally achieved and correlated with chemical analysis by atom probe tomography and the point defects quantification using positron annihilation spectroscopy.

The development of the WB-STEM and its application to RPV steel have been applauded in the journal *Microscopy* as a key technology for visualizing lattice defects (Fig. 1(b)) [1]. In 2017, the WB-STEM contributed to two Ph.D theses and 10+ research projects from home and abroad as a common facility in the Oarai center.

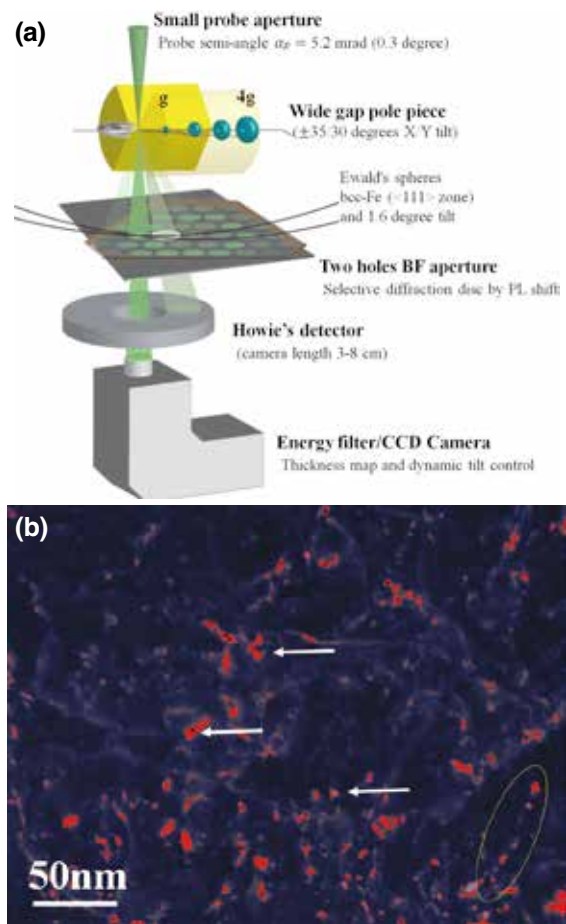


Fig. 1 (a) Schematic of the WB-STEM, which consists of a small probe aperture, wide-gap pole piece, two-hole BF aperture, annular detector and CCD camera. (b) WB-STEM image of RPV steel with  $(g, 3g)$ ,  $g = 1-10$ . The arrows and ellipse indicate small dislocation loops and loops that lie on a dislocation, respectively.

## References

- [1] K. Yoshida, M. Shimodaira, T. Toyama, Y. Shimizu, K. Inoue, T. Yoshiie, K. J. Milan, R. Gerard, and Y. Nagai, *Microsc.* **66**, 120 (2017).

Kenta Yoshida (Corresponding Author, International Research Center for Nuclear Materials Science)

E-mail: k\_yoshida@imr.tohoku.ac.jp

Yasuyoshi Nagai (Head of International Research Center for Nuclear Materials Science)

E-mail: nagai@imr.tohoku.ac.jp

URL: <http://www.imr-oarai.jp/>

# Switching of Magnetic Ordering in Uranium Intermetallic Compound $U(\text{Ir}_{1-x}\text{Rh}_x)\text{Ge}$

International Research Center for Nuclear Materials Science

The evolution of magnetic ordering in intermetallic uranium compounds is studied. An antiferromagnetic ground state of  $\text{UIrGe}$  is shown to suddenly transformed to a ferromagnetic one by the substitution of Ir by Rh. The resulting density of states is highly different in the ferromagnetic and antiferromagnetic ground states.

Uranium intermetallic compounds with an orthorhombic  $\text{TiNiSi}$ -type crystal structure are attracting attention because two of the compounds belonging to this family,  $\text{UCoGe}$  and  $\text{URhGe}$ , are known as ferromagnetic superconductors. On the contrary, isostructural and isoelectronic  $\text{UIrGe}$  is an antiferromagnet without superconductivity down to 50 mK, even for an extremely high-quality single crystal [1]. It is suggested that ferromagnetism in these compounds is essential for realizing superconductivity. But how can the ferromagnetic ordering be stabilized in these compounds?

We studied the evolution of magnetic ground states this system by substituting transition metal sites [2]. In  $\text{UTGe}$  ( $T = \text{Co, Rh, and Ir}$ ), magnetism is dominated by the uranium 5f electrons. Transition metals are almost magnetically inert. It is therefore expected that the substitution of the transition metal sites would exert chemical pressure. Figure 1 shows the magnetic phase diagram in the  $U(\text{Ir}_{1-x}\text{Rh}_x)\text{Ge}$  alloy. For comparison, the result for  $U(\text{Co}_{1-x}\text{Rh}_x)\text{Ge}$  [3] is also shown. The transition temperatures are plotted as a function of the interatomic distance of neighboring uranium atoms  $d_{\text{U-U}}$  [4]. Although  $d_{\text{U-U}}$  changes only gradually, the magnetic transition temperature changes drastically upon substitution. More interestingly, the antiferromagnetic (AFM) ground state of  $\text{UIrGe}$  switches to a ferromagnetic (FM) state suddenly at the critical composition  $U(\text{Ir}_{0.44}\text{Rh}_{0.56})\text{Ge}$ . Precise experiments near the critical composition have shown that the AFM/FM transition is of the first order. This result demonstrates that a slight modification of  $d_{\text{U-U}}$  can even change the magnetic structure. Fig. 2 shows a plot of the electronic specific heat coefficient  $\gamma$  in the ordered state.  $\gamma$  in the FM phase is almost independent of the substitution showing values as large as typical heavy fermion materials. In AFM, however,  $\gamma$  is significantly reduced. This suggests that the AFM ordering exhausts the majority of electronic entropy, leaving a relatively low electronic density of states at

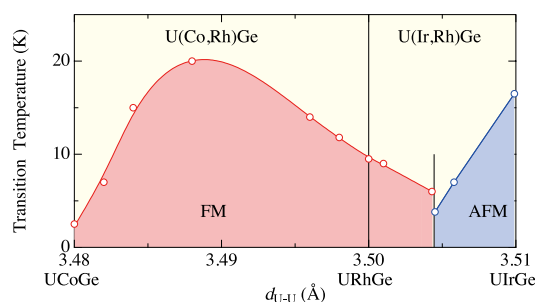


Fig. 1 Magnetic transition temperature of  $U(\text{Rh, Ir})\text{Ge}$  and  $U(\text{Co, Rh})\text{Ge}$  alloys. The horizontal axis is the interatomic distance between neighboring uranium atoms [4].

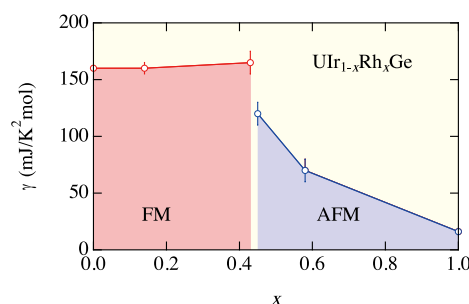


Fig. 2 Electronic specific heat coefficient of  $U(\text{Rh, Ir})\text{Ge}$ .

the Fermi energy.

This demonstrates that the FM and AFM states are equally stable in this system, but the resulting ground state density of states is significantly different. The results suggest the importance of a highly enhanced density of states in the FM ground state for superconductivity in  $\text{UCoGe}$  and  $\text{URhGe}$ .

## References

- [1] J. Pospíšil, J. Gouchi, Y. Haga, F. Honda, Y. Uwatoko, N. Tateiwa, S. Kambe, S. Nagasaki, Y. Homma, and E. Yamamoto, *J. Phys. Soc. Jpn.* **86**, 044709 (2017).
- [2] J. Pospíšil, Y. Haga, S. Kambe, Y. Tokunaga, N. Tateiwa, D. Aoki, F. Honda, A. Nakamura, Y. Homma, E. Yamamoto, and T. Yamamura, *Phys. Rev. B* **95**, 155138 (2017).
- [3] N. Huy and A. de Visser, *Solid State Commun.* **149**, 703 (2009).
- [4] D. Aoki and J. Flouquet, *J. Phys. Soc. Jpn.* **81**, 011003 (2012).

Yoshinori Haga (Corresponding Author, Advanced Science Research Center, JAEA)

E-mail: haga.yoshinori@jaea.go.jp

Yasuyoshi Nagai (Head of International Research Center for Nuclear Materials Science)

E-mail: nagai@imr.tohoku.ac.jp

URL: <http://www.imr-oarai.jp/>

# High-Performance Ni<sub>3</sub>(Al, V) L<sub>12</sub> Intermetallic-Based Alloys as High-Temperature Structural Materials

Cooperative Research and Development Center for Advanced Materials

The Center contributes to research and development of new materials and their fabrication processes in order to explore the possibility of their application as multifunctional materials for future technology under collaboration with universities and government organizations. Here, we highlight our recent activity of investigating the mechanical properties of the novel Ni<sub>3</sub>(Al, V) L<sub>12</sub> intermetallic-based alloys in the field of high-temperature structural materials.

The center has developed novel materials and processes under collaboration with universities and government organizations. One of these is the research on Ni<sub>3</sub>(Al, V) L<sub>12</sub> intermetallic-based alloys, which have been investigated by our center and Osaka Prefecture University [1-4].

The Ni<sub>3</sub>(Al, V) alloys, which have a single phase of ordered L<sub>12</sub> cubic structure with a composition of Ni-13 at.% Al-12 at.% V, are fabricated by solution-treatment at a high temperature of 1050 °C and then quenched in water. The Ni<sub>3</sub>(Al, V) alloys exhibit superior mechanical strength and ductility at high temperatures (Fig. 1). The fractural elongation of the alloys exceeded 20% at room temperature and above 5% even at 800 °C, which is considerably superior to conventional Ni<sub>3</sub>Al intermetallic alloys. Additionally, the yield strength of the Ni<sub>3</sub>(Al, V) alloys increases with increasing temperature (referred to as “the anomalous temperature dependency of yielding”), which is desirable property for high-temperature applications.

It was also found that both the strength and ductility of the Ni<sub>3</sub>(Al, V) alloys can be further improved by aging after quenching, which is caused by an age-induced precipitation hardening effect. Figure 2 shows a TEM image of the Ni<sub>3</sub>(Al, V) alloys aged isothermally at 850 °C. A number of fine precipitates of Ni<sub>3</sub>V D0<sub>22</sub> (tetragonal structure,  $a = 0.381$  nm,  $c = 0.592$  nm) were formed coherently on the {001} planes of the Ni<sub>3</sub>(Al, V) L<sub>12</sub> (cubic,  $a = 0.373$  nm) matrix. The number and size of the plate-shaped Ni<sub>3</sub>V precipitates increased gradually with increasing aging time.

Thus, a proper design of the alloy composition and thermomechanical process for the Ni<sub>3</sub>(Al, V) alloys are required to enhance their mechanical strength and ductility at an elevated temperature. The detailed findings to control the microstructure and mechanical properties will be reported in the near future.

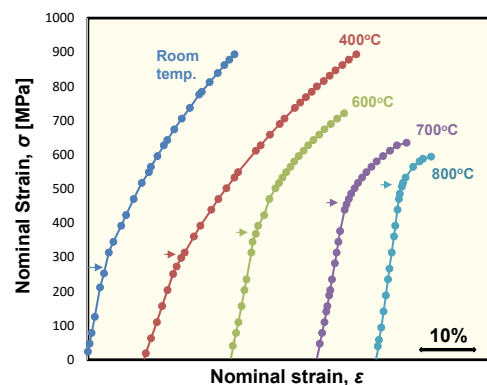


Fig. 1 Tensile stress–strain curves for the Ni<sub>3</sub>(Al, V) alloy from room temperature to 800 °C. The 0.2% yield stress is marked by arrows.

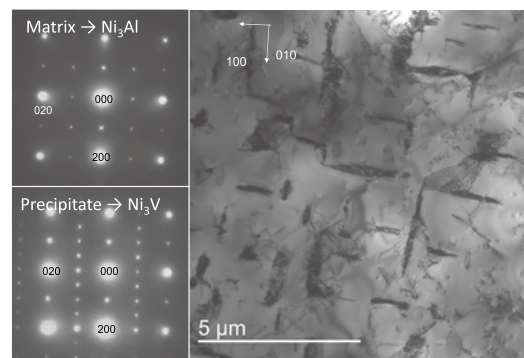


Fig. 2 Bright-field TEM images and selected-area electron diffraction patterns taken from the matrix and precipitates in the Ni<sub>3</sub>(Al, V) alloy aged at 850 °C for 48 h.

## References

- [1] D. Edatsugi, Y. Kaneno, S. Semboshi, and T. Takasugi, *Metall. Mater. Trans. A*, **47**, 998 (2016).
- [2] S. Semboshi, H. Tsuda, Y. Kanano, A. Iwase, and T. Takasugi, *Intermetallics*, **59**, 1 (2015).
- [3] R. Sasaki, S. Semboshi, M. Nagasako, Y. Kaneno, A. Iwase, and T. Takasugi, 2016 MRS Fall Meeting, Boston, USA, 2016.
- [4] R. Sasaki, Master's thesis in Osaka Pref. Univ. (2017).

Satoshi Semboshi (Corresponding Author, Cooperative Research and Development Center for Advanced Materials)

E-mail: semboshi@imr.tohoku.ac.jp

Tadashi Furuhashi (Head of Cooperative Research and Development Center for Advanced Materials)

E-mail: crdam@imr.tohoku.ac.jp

URL: <http://www.crdam.imr.tohoku.ac.jp/ja/index.html>

# Robust Emergent-Monopole Fluctuations as a Source of Large Thermoelectric Conversion

High Field Laboratory for Superconducting Materials

Hairy magnetic structures with nontrivial topology, so-called spin hedgehogs, behave as emergent monopoles, which affect the motion of conduction electrons in various ways. By exploiting steady magnetic fields of a 25 T cryogen-free superconducting magnet, we have identified that robust fluctuations of emergent monopoles play a key role in the large thermoelectric effect persisting up to high magnetic fields in a chiral magnet MnGe.

Complex electronic orders are a fertile source of emergent electromagnetic responses, the origins of which depend on the geometry of the assembled constituents and their collective behavior. Relevant examples include a variety of topological spin textures, such as solitons, skyrmions, and hedgehogs; they exhibit rich transport and magnetoelectric properties via transcribing the geometry of each spin ensemble to the electronic states [1]. In particular, the unique three-dimensional spin arrangement of hedgehogs produces a quantized source and sink of an effective gauge field, that is, emergent monopoles (Fig. 1(a)). Because of their fluctuations and consequent considerable dynamical variation in the emergent magnetic field distribution, the charge carriers get scattered, acquiring large entropy.

Here, we experimentally identify the origin of an unusually enhanced thermopower by the application of magnetic field in MnGe with a spin-hedgehog lattice as the emergent monopoles' fluctuations [2]. Through high-field measurements of the thermoelectric effect (Seebeck effect) in the 25 T cryogen-free superconducting magnet (25 T-CSM) installed at IMR, Tohoku University, we revealed that their strong fluctuations—the source of large entropy and thus thermopower—can remain at high magnetic fields above 10 K, and eventually quenched below 5 K (Fig. 1(b)).

The observed robustness is possibly rooted in topological protection against unwinding of the spin texture by external magnetic fields; this property could be captured only by utilizing the steady high magnetic fields of the 25 T-CSM. The present results not only open the door to efficient thermoelectric conversion in topological magnets, but also demonstrate the promising usefulness of high-field measurements to clarify the topological stability of spin nano-objects.

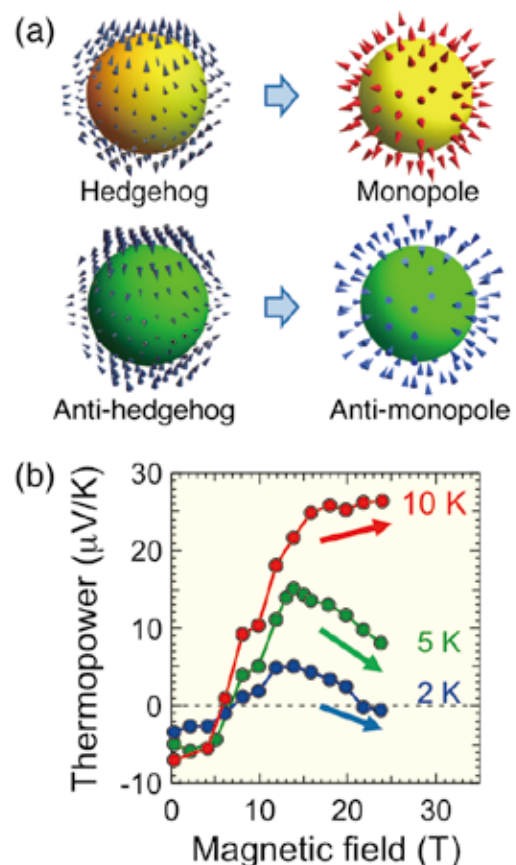


Fig. 1 (a) Spin hedgehogs and corresponding emergent field distributions (emergent monopoles). (b) Magnetic field dependence of thermopower at 2, 5, and 10 K.

## References

- [1] N. Kanazawa, S. Seki, and Y. Tokura, *Adv. Mater.* **29**, 1603227 (2017).
- [2] Y. Fujishiro, N. Kanazawa, T. Shimojima, A. Nakamura, K. Ishizaka, T. Koretsune, R. Arita, A. Miyake, H. Mitamura, K. Akiba, M. Tokunaga, J. Shiozaki, S. Kimura, S. Awaji, A. Tsukazaki, A. Kikkawa, Y. Taguchi, and Y. Tokura, *Nat. Commun.* **9**, 408 (2018).

Naoya Kanazawa (Corresponding Author, Department of Applied Physics, School of Engineering, The University of Tokyo)

E-mail: kanazawa@ap.t.u-tokyo.ac.jp

Hiroyuki Nojiri (Head of High Field Laboratory for Superconducting Materials)

E-mail: nojiri@imr.tohoku.ac.jp

URL: <http://www.hflsm.imr.tohoku.ac.jp/>

## Scientific Breakthrough Toward Creation of New Industrial Materials

### Trans-Regional Corporation Center for Industrial Materials Research

Institute for Materials Research (IMR) has launched the Trans-Regional Corporation Center, a comprehensive Institute-wide effort that pairs IMR's research groups across the innovation spectrum to solve today's industrial challenges and transform tomorrow's global energy problems. The center was established in April 2016 based on an agreement between IMR, the Osaka Prefecture Government, and enterprises in the Kansai area sponsored by government, taking over Osaka and Kansai center projects.

The Trans-Regional Corporation Center was established in Osaka as a special unit in the Institute for Materials Research (IMR), Tohoku University in April 2016 based on an agreement with the Osaka Prefecture Government. The center is sponsored by the government (Ministry of Education, Culture, Sports, Science and Technology) and took over the Kansai Center, which carried out its mission from 2012 to 2016. The Trans-Regional Corporation Center has three missions. First, to solve technical problems that industrial stakeholders have struggled to resolve. Second, the center introduces academic output to industries, with the aim of applying such output to society. Third, the center helps to educate next-generation materials scientists and researchers in universities and enterprises. We have organized a bimonthly forum named "Monodukuri Kisokoza," which focuses on special topics regarding materials and processing. Projects are conducted through wide collaborations between the government, universities, research institutions, and other organizations. The center has four venues to cover the Kansai area: the Osaka office at Osaka Prefecture University, the Hyogo office at the University of Hyogo, the Sendai office in IMR, and the Monozukuri Business Information Center Osaka (MOBIO) in the Creation Core Higashi-Osaka, a governmental body in which fifteen local universities and one college are located to facilitate collaboration with various industries.

The center has developed materials and processes under collaboration with industries, universities, and government organizations. One of these is a consolidation process of metallic glass powders, which has been developed by IMR and Porite Co., LTD under the strategic core technology advancement program of Ministry of Economy, Trade and Industry (METI). The Ni-Cr-Nb-P-B metallic glasses (Ni-MGs) exhibit high glass forming ability, high yield strength, and high corrosion resistance. No crystalline particles were observed in the gas atomized Ni-MG powders with diameter below 53  $\mu\text{m}$ , even with the use of low-grade raw material. In order that back extrusion and high heating rate consolidation process applies large

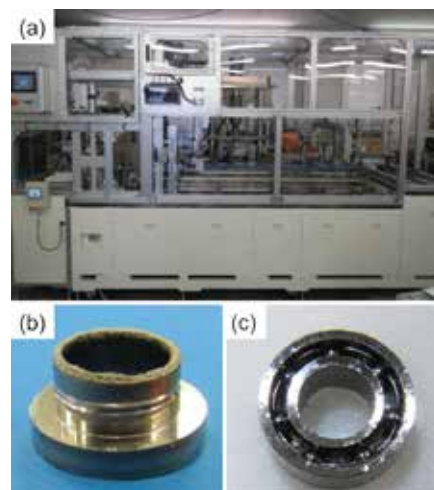


Fig. 1 (a) Automatic and high-rates consolidation system for MGs, (b) the extruded sample of Ni-MG, (c) the trial components of miniature bearing (O.D. = 6.35 mm, I.D. = 3.175 mm) with Ni-MG. The inner and outer bearing races are manufactured by the consolidation process of Ni-MG powders.

shearing to powder with low viscosity, the Ni-MGs indicate good consolidation. Furthermore, the automatic and high-rates powder consolidation system for MGs with no vacuum was also developed [Fig. 1(a)], and can carry out consolidation of 60 parts per hour of Ni-MG. A miniature bearing with Ni-MG [1] was demonstrated as the results of development [Fig. 1 (b, c)].

Similar collaboration research studies for practical applications utilizing academic knowledge and industrial technology are in progress. The Trans-Regional Corporation Center will endeavor to innovate in the metallic material industry through the alliance with partners in the Kansai area, and promote research of materials science.

#### References

- [1] F. Habuki, Y. Saotome, K. Amiya, N. Shimada, A. Okuma, T. Iwasaki, and H. Kimura, Japan Patent Publication number 2017-122510, Date of filing 2017-7-13.

Kenji Amiya (Corresponding Author, Trans-Regional Corporation Center for Industrial Materials Research)

E-mail: [amiya.k@imr.tohoku.ac.jp](mailto:amiya.k@imr.tohoku.ac.jp)

Naoya Masahashi (Head of Trans-Regional Corporation Center for Industrial Materials Research)

E-mail: [masahasi@imr.tohoku.ac.jp](mailto:masahasi@imr.tohoku.ac.jp)

URL: <http://www.trc-center.imr.tohoku.ac.jp/>

# Supercomputing to Understand Materials Properties

Center for Computational Materials Science

The Center for Computational Materials Science supports various advanced studies on computational materials science by providing users with an efficiently tuned high-performance computer. We introduce two major activities selected from approximately 120 users. Dr. Tsukahara and Dr. Ono investigate the properties of isotropic nanocrystalline permanent magnets. Dr. Takahashi investigates the terahertz-spectral property of nicotinamide, focusing on the temperature.

## Magnetization Reversal Processes of Isotropic Permanent Magnets with Various Intergrain Exchange Interactions <sup>a)</sup>

A permanent magnet is a key material for high-efficiency power motors, which are essential for electric vehicles. However, the coercivity of real magnets is much smaller than the theoretical value. We performed large-scale micromagnetic simulations to reveal the discrepancy between the actual and theoretical coercivity using a simple simulation model, as shown in Fig. 1(a). Figure 1(b) shows the coercivity of the simulation models as a function of the intergrain exchange interaction parallel and perpendicular to the external field [1]. When the intergrain exchange interaction acts only parallel to the external field (type A), the degradation of the coercivity is the smallest. In contrast, the coercivities are strongly degraded with increasing the intergrain exchange interaction parallel to the external field (type B) and all directions (type O).

## Temperature Dependence in the Terahertz Spectrum of Nicotinamide: Anharmonicity and Hydrogen-Bonded Network <sup>b)</sup>

By analyzing the terahertz (THz) spectrum of nicotinamide with dispersion-corrected density functional theory calculations, we recently found that the difference in the temperature-dependent peak shift is well understood in terms of the presence/absence of stretching vibration of the intermolecular hydrogen bond (Fig. 2) in the mode and the change in cell parameters [2]. Almost all peaks in the THz spectrum showed a remarkable peak shift with temperature, whereas the lowest-frequency peak showed a negligible shift. The anharmonicity in the dissociation potential energy of very weak intermolecular hydrogen bonds causes the remarkable peak shift. The stationary feature of the lowest-frequency peak is explained by combining two effects, that giving the opposite

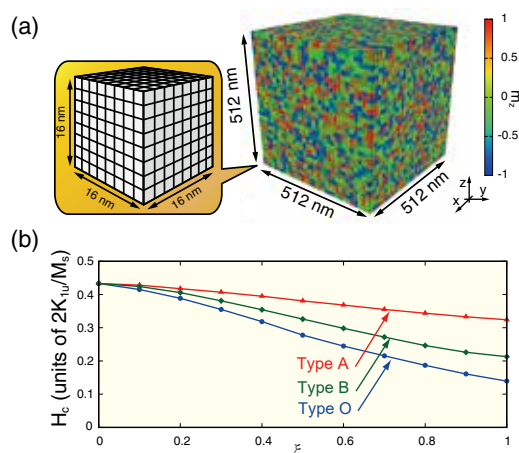


Fig. 1 (a) Schematic of the isotropic nanocrystalline permanent magnet model. (b) Coercive force  $H_c$  as a function of the strength of the intergrain exchange interaction  $\xi$ .

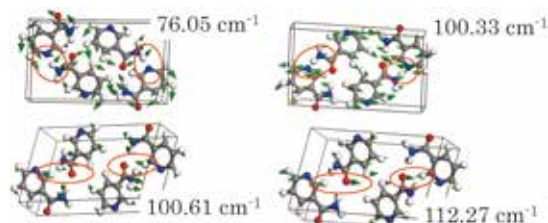


Fig. 2 Calculated vibrational modes with intermolecular weak hydrogen-bond stretches.

frequency shift to low frequency due to the volume expansion and that to high frequency due to the intermolecular or interatomic repulsions.

## References

- [1] H. Tsukahara, K. Iwano, C. Mitsumata, T. Ishikawa, and K. Ono, *AIP Adv.* **7**, 056224 (2017).
- [2] M. Takahashi, N. Okamura, X. Fan, H. Shirakawa, and H. Minamide, *J. Phys. Chem. A* **121**, 2558 (2017).

a) Hiroshi Tsukahara (Corresponding Author, High Energy Accelerator Research Organization) and Kanta Ono (High Energy Accelerator Research Organization)

E-mail: thiroshi@post.kek.jp

b) Masae Takahashi (Corresponding Author, Graduate School of Agricultural Science, Tohoku University)

E-mail: masae@fris.tohoku.ac.jp

Momiji Kubo (Head of Center for Computational Materials Science)

URL: <http://www.ccms.imr.tohoku.ac.jp/Eng/>

## Interaction of Grain Boundaries at Crystal/Melt Interface of Silicon

### Collaborative Research Center on Energy Materials

What will happen when two grain boundaries meet at a crystal/melt interface? To answer this question, we directly observe the crystal/melt interface of multicrystalline silicon during directional solidification.

Multicrystalline silicon (mc-Si) grown through directional solidification is the dominant material in photovoltaic applications. A grain boundary (GB) in mc-Si is one of the most significant factors deteriorating the conversion efficiency of solar cells. However, the behaviors of GBs at a crystal/melt interface have not been well understood, especially with respect to the interaction between two GBs. Therefore, in this study, we have attempted to elucidate mechanisms behind GB interactions through *in-situ* observations during crystal growth.

Experiments were performed using an *in-situ* observation system consisting of a microscope and a crystallization furnace. The solidified silicon crystal samples were analyzed using electron backscattering diffraction (EBSD) to determine the grain orientations and structure of the GBs.

Figure 1 shows a crystal/melt interface of mc-Si during directional solidification, and Figure 2 shows the results of EBSD analysis of the observed area. Several grain boundaries, including small-angle grain boundary (SAGB) and  $\Sigma 3$  GB were observed in the growing crystal. A pair of straight  $\{111\}\Sigma 3$  GBs, confirmed by EBSD measurement (see Fig. 2(b-d)), grow slanting toward the lower-left region of the figure. This pair of  $\{111\}\Sigma 3$  GBs met another pair growing from the lower part (Fig. 1(4)). Fig. 2(c) shows the convergence of two pairs of  $\{111\}\Sigma 3$  GBs to produce a new  $\Sigma 9$  GB. This  $\Sigma 9$  GB later converged with a  $\{111\}\Sigma 3$  GB to form a new  $\{111\}\Sigma 3$  GB with a different growth direction, as shown in Fig. 2(c).

In contrast to this situation,  $\Sigma 3$  GBs did not interact with SAGBs during the solidification. From the *in-situ* observation snapshots shown in Fig. 1(3) and 1(4), the SAGBs grew through the  $\{111\}\Sigma 3$  GBs without changing their direction of growth. This was confirmed by EBSD analysis, as shown in Fig. 2(d). The misorientation of SAGB did not change before and after the interactions with  $\Sigma 3$  GBs.

We also observed the interaction between two SAGBs, as shown in Fig. 2(e).  $SAGB_1$  and  $SAGB_2$  converge and only one GB with a slightly higher misorientation, referred to as  $SAGB_3$ , remains.

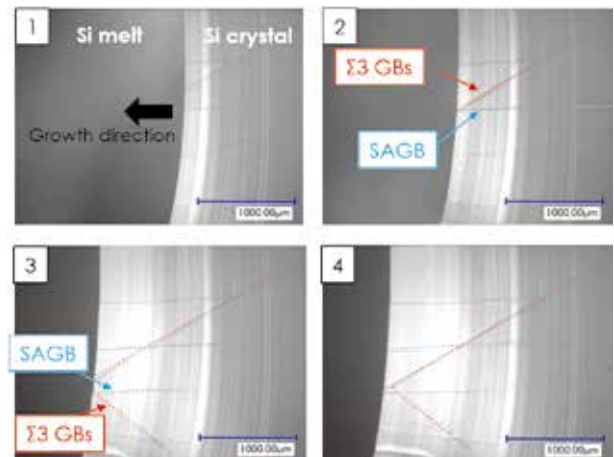


Fig. 1 Observation of interaction between GBs at crystal/melt interface in Si.

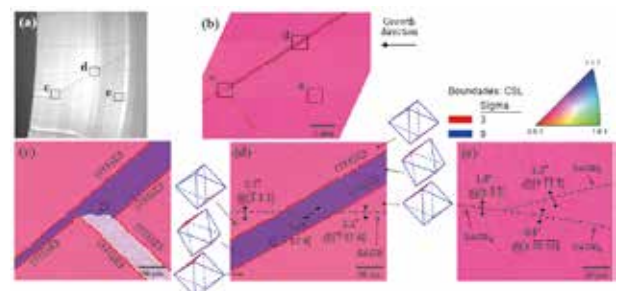


Fig. 2 EBSD analysis for characterization of observed GBs.

In this way, usually, when two GBs meet at a crystal/melt interface, a new GB is established (e.g.,  $\Sigma 3 + \Sigma 3 \rightarrow \Sigma 9$  and  $SAGB + SAGB \rightarrow SAGB$ ). However, interestingly, no such reaction occurs between SAGB and  $\Sigma 3$  GB, i.e.,  $\Sigma 3 + SAGB \rightarrow \Sigma 3 + SAGB$ , with no change of misorientation and direction.

#### References

- [1] L-C. Chuang, K. Maeda, H. Morito, K. Shiga, W. Miller, and K. Fujiwara, *Scr. Mater.* **148**, 37 (2018).

Kozo Fujiwara (Corresponding Author, Collaborative Research Center on Energy Materials/Crystal Physics Division)

E-mail: kozo@imr.tohoku.ac.jp

Shin-ichi Orimo (Head of Collaborative Research Center on Energy Materials)

E-mail: orimo@imr.tohoku.ac.jp

URL: <http://www.e-imr.imr.tohoku.ac.jp/>

# Investigation of Magnon Spin Valve Effects in Insulator Spintronics

## International Collaboration Center (ICC-IMR)

Information transport and processing by pure magnonic spin currents in insulators is a promising alternative to conventional charge-current driven spintronic devices due to reduced ohmic losses. During the stay at ICC-IMR, magnetization orientation dependent detection of magnon spin currents was studied in  $\text{Y}_3\text{Fe}_5\text{O}_{12}$  (YIG)|CoO|Co tri-layers. The detected spin signal depends on the relative alignment of the YIG and Co magnetization. This demonstrates a magnon spin valve behavior with an effect amplitude of >120%.

In Fig. 1(a) the YIG/CoO/Co multilayer sample is schematically shown [1]. After determining the magnetic properties of YIG and Co, we study the magnon spin current detection as a function of the YIG and Co alignment. Figures 1(c-f) show field-dependent voltage signals induced by  $f = 4.5$  GHz microwave irradiation at  $T = 120$  K. By means of specific field sweep sequences, parallel (d, e) as well as anti-parallel (c, f) alignment of YIG and Co is realized. In the parallel state (Fig. 1(d, e)) a multipeak voltage signal appears corresponding to two overlapping Lorentzian line shapes of opposite sign. In the antiparallel state (Fig. 1(c, f)) a voltage peak of one polarity but with a significant asymmetry is observed, which can be fitted by two overlapping Lorentzian functions.

The comparison of all four datasets allows us to separate and attribute the peaks to different effects: (i)

the signal of the spin current generated in the YIG and detected in the Co ( $V_{sc}$ , blue curves) and (ii) a second signal that originates from the Co ( $V_{sr}$ , green curves) and potentially is due to spin rectification (SR).

The intriguing discovery in this experiment is the alignment-dependent amplitude of  $V_{sc}$  analogous to the spin-polarized charge current transmission in a conventional spin valve. While  $V_{sr}$  is independent of the relative alignment of the layers, the amplitude of  $V_{sc}$  is about 120% larger in the antiparallel state as compared to the parallel state. Regarding the total voltage  $V_{sc+sr}$ , a signal amplitude variation of up to 290% is observed.

### References

- [1] J. Cramer, F. Fuhrmann, U. Ritzmann, V. Gall, T. Niizeki, R. Ramos, Z. Qiu, D. Hou, T. Kikkawa, J. Sinova, U. Nowak, E. Saitoh, and Mathias Kläui, Nat. Commun. **9**, 1089 (2018).

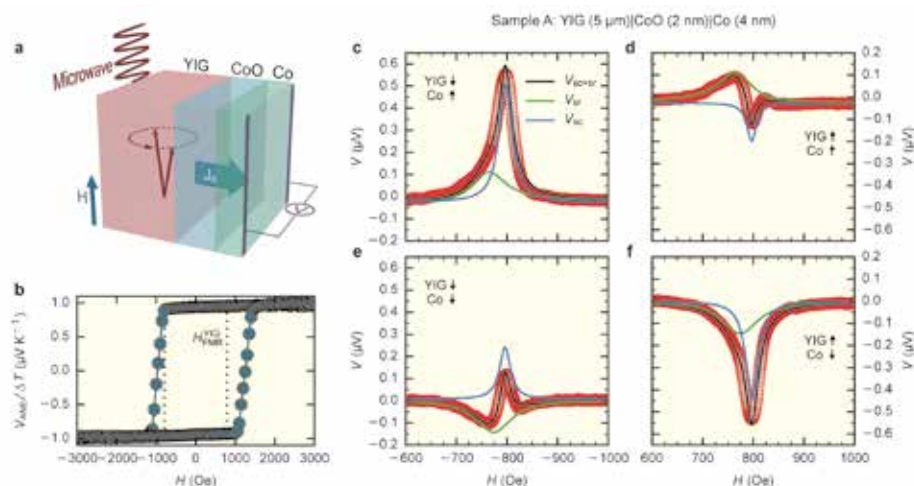


Fig. 1 (a) Illustration of the investigated YIG|CoO|Co tri-layer system. A spin current  $J_s$  induced in the YIG by FMR spin pumping, propagates through the CoO layer and is detected electrically in the Co layer via the inverse spin Hall effect. The relative magnetization orientation of YIG and Co can be adjusted to be either parallel or antiparallel. (b) Typical anomalous Nernst effect hysteresis loop observed at  $T = 120$  K (field cooled at  $H_{ext} = 90$  kOe). (d)-(f) Field-dependent voltage signals detected induced by microwave irradiation. The total signal is given by a superposition of two distinct signals  $V_{sc}$  and  $V_{sr}$ , the sign of which individually depend on the YIG and Co orientation. The amplitude of  $V_{sc}$  furthermore depends on the relative alignment of YIG and Co. (From [1])

Mathias Kläui (Corresponding Author, Johannes Gutenberg University Mainz)

E-mail: [Klaeui@uni-mainz.de](mailto:Klaeui@uni-mainz.de)

<http://www.klaeui-lab.de>

Gerrit Ernst-Wilhelm Bauer (Head of International Collaboration Center)

E-mail: [icc-imr@imr.tohoku.ac.jp](mailto:icc-imr@imr.tohoku.ac.jp)

URL: <http://www.icc-imr.imr.tohoku.ac.jp/>

## Neutrons for Advanced Materials Science

### Center of Neutron Science for Advanced Materials

The Center of Neutron Science for Advanced Materials is a neutron facility, which has a background of novel materials science in IMR. This center operates three neutron instruments in a research reactor facility JRR-3 under a general user program, and is now constructing a state-of-the-art neutron spectrometer at J-PARC/MLF. We hope to contribute to the development of materials science and neutron science by utilizing the unique platform of the neutron instruments.

The Center of Neutron Science for Advanced Materials (CN-IMR) was established in 2010 with the aim of promoting novel materials science by using neutrons. The CN-IMR operates two neutron spectrometers and one diffractometer at the JRR-3 research reactor in the Japan Atomic Energy Agency and is now constructing a state-of-the-art polarized neutron spectrometer, POLANO, with an intense neutron source at the Materials and Life Science Experimental Facility (MLF) in the Japan Proton Accelerator Research Complex (J-PARC) [1,2]. POLANO will achieve polarization analysis in higher energy regions beyond the measurements performed by a triple-axis spectrometer at a reactor-based neutron source, and thereby, provide a huge opportunity for research in the field of strongly correlated electron systems. The construction of POLANO started in 2012 under the collaboration with the High Energy Accelerator Research Organization (KEK). After the construction of the main part of the instruments, we have finally succeeded in receiving the first neutron beam at POLANO on 21 June. The spectrometer will be offered for the collaborative research programs of IMR after the commissioning process.

In order to discuss future neutron research brought through new materials and the unique instruments at J-PARC and JRR-3, including POLANO, we held a two-day workshop, "Complementary use of J-PARC and JRR-3 in Neutron Science Research." Approximately fifty material and neutron scientists attended the workshop and exchanged information. The strategic use of the neutron facility and neutron instrument was also discussed. The workshop was well received by the participants. Furthermore, to promote the utilization of neutrons for condensed matter physics and materials science, we distributed leaflets for the advertisement of our spectrometers to the participants as well as research groups in Japan.



Fig. 1 Photograph of some of the POLANO project members. We have succeeded in receiving the first neutron beam at POLANO installed in J-PARC/MLF.



Fig. 2 Photograph of workshop held in IMR. More than forty scientists participated and discussed the future neutron science.

#### References

- [1] T. Ino, M. Ohkawara, K. Ohoyama, T. Yokoo, S. Itoh, Y. Nambu, M. Fujita, H. Kira, H. Hayashida, K. Hiroi, K. Sakai, T. Oku, and K. Kakurai, *J. Phys. Conf. Ser.* 862, 012011/1-012011/11 (2017).
- [2] M. Ohkawara, T. Ino, Y. Ikeda, T. Yokoo, S. Itoh, K. Ohoyama, and M. Fujita, *J. Phys. Conf. Ser.*, (2018) in press.

Masaki Fujita (Head of Center of Neutron Science for Advanced Materials)

E-mail: [nc-imr@imr.tohoku.ac.jp](mailto:nc-imr@imr.tohoku.ac.jp)

URL: <http://nc-imr.imr.tohoku.ac.jp/>

# Quantum Fluctuation-Dominated States in Highly Crystalline Two-Dimensional Superconductors

Laboratory of Low Temperature Materials Science

Two-dimensional (2D) superconductors with high crystallinity have been new platforms for the novel quantum phenomena. Here, we provide a universal field versus temperature phase diagram of such clean 2D superconductors, including a variety of quantum fluctuation-dominated states and quantum phase transitions, which is totally different from that of conventional or dirty 2D superconductors, by using gate-induced electron systems.

Two-dimensional (2D) superconductors have been well-known platforms for the study of a quantum phase transition (QPT) occurring at zero temperature. The superconductor–insulator transition (SIT) tuned by magnetic field is one of the remarkable phenomena of QPT. Such a QPT was predominantly investigated in dirty superconductors in the form of granular or amorphous thin films, because the localization effect of superconducting electrons or vortices by disorder plays a significant role for SIT. However, it has been long argued how the QPT and the quantum phases evolve with the weakening of the effect of disorder. Recently, our group found that the gate-induced superconducting surface of a ZrNCl single crystal indicates the quantum metallic/vortex liquid state with non-zero electrical resistance by applying a very small field far below the mean field critical field  $B_{c2}^{MF}$  at the low temperature limit [1]. Thus, the conventional picture for the field-induced SIT needs to be modified, and the transition from the quantum metallic state to the normal state at low temperature emerges as a new subject of the QPTs in highly crystalline 2D superconductors with minimal disorder.

Here, we propose a comprehensive field – temperature ( $B$ – $T$ ) phase diagram of highly crystalline 2D superconductors, which is composed of two thermal fluctuation regions and two quantum fluctuation regions, as shown in Fig. 1. Based on detailed analyses of magneto-transport properties in ion-gated ZrNCl and MoS<sub>2</sub>, we found that these 2D superconducting systems commonly show a wide range of a quantum phase stemming from the very low magnetic field at low temperature, which transfer to the weakly localized metal through the quantum critical point (QCP). In particular, the observed QPT has a character known as the quantum Griffiths singularity with the critical exponent diverging toward the QCP, which is distinct from that of the conventional

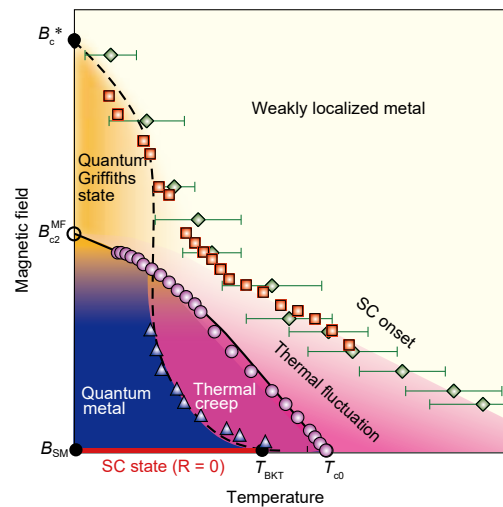


Fig. 1 Magnetic field vs. temperature ( $B$ – $T$ ) phase diagram of highly crystalline 2D superconductors [2].  $T_{c0}$  is the mean field transition temperature and  $T_{BKT}$  is the Berezinskii–Kosterlitz–Thouless temperature. The data points are various crossover temperatures or fields obtained from the analyses of resistive transition curves.

SIT with a constant exponent. This implies that the critical state (quantum Griffiths state) below the QCP is described by so-called rare regions, interpreted as superconducting puddles surviving in the normal state background at  $T \rightarrow 0$  K.

The present result strongly indicates that quantum fluctuation dominates the wide quantum metallic state and its crossover to the quantum Griffiths state, which appears as a generic feature of highly crystalline 2D superconductors.

## References

- [1] Y. Saito, Y. Kasahara, J. Ye, Y. Iwasa, and T. Nojima, *Science*, **350**, 409 (2015).
- [2] Y. Saito, T. Nojima, and Y. Iwasa, *Nat. Commun.* **9**, 778 (2018).

Tsutomu Nojima (Corresponding Author, Laboratory of Low Temperature Materials Science)

E-mail: nojima@imr.tohoku.ac.jp

Takahiko Sasaki (Head of Laboratory of Low Temperature Materials Science)

E-mail: takahiko@imr.tohoku.ac.jp

URL: <http://ltsd.imr.tohoku.ac.jp/>

# Research Facility for Physics and Chemistry of Radioactive and Nuclear Materials

## Laboratory of Alpha-Ray Emitters

More than 170 species of radioisotopes and nuclear materials are available for study at the Laboratory of Alpha-ray Emitters. This laboratory is one of the most important centers around the world for studying the physical and chemical properties of radioactive materials, such as actinide compounds. Researchers from many of the leading universities and institutes all over the country visit this facility every year to prepare a variety of materials and carry out chemical and physical measurements.

The Laboratory of Alpha-Ray Emitters provides a research environment for the study of 170 radionuclides (RIs) and elements, especially alpha-ray emitters such as actinides. This laboratory functions as a source for the preparation of pure crystals of actinide compounds, providing them to other universities and to Synchrotron Orbital Radiations (SORs). The Radiation Controlled Area of this laboratory includes three chemistry labs and three physical labs, which are equipped with local exhaust ventilation systems enabling the handling of various types of materials. Many spectrometers including those for gamma-rays and alpha-rays are available.

Recently, lanthanide or uranium-based single-molecule magnets (SMMs) have attracted much attention [1, 2]. In these compounds, the large magnetic anisotropy and the strong spin-orbit interaction reduce the rate of magnetic relaxations. In most uranium-based SMMs, uranium (III) is used instead of uranium (IV). However, it is important to study the magnetization of uranium (IV) complexes to understand the relationship between magnetic anisotropy and magnetic relaxations. In this study, we aim to observe slow magnetic relaxations on bisphthalocyaninato-uranium (IV) complex ( $\text{UC}_6\text{H}_4\text{N}_8$ ) as an SMM example of an  $f^2$  system. This complex has an identical structure to that of the well-studied bisphthalocyaninato-lanthanide complexes, such that we can compare the actinide-based SMM with lanthanide-based SMMs.

As a precursor of uranium (IV), we prepared  $\text{UCl}_4$ . A mixture of  $\text{UCl}_4$  and phthalonitrile ( $\text{C}_6\text{H}_4(\text{CN})_2$ ) in a 1:10 molar ratio in a glass test tube was purged with Ar, and heated to  $250^\circ\text{C}$ . A dark-green solid obtained, washed with water and ethanol, and then dried under vacuum. The crude product was placed in a quartz tube, evacuated to  $10^{-3}$  Torr and heated to  $450^\circ\text{C}$ . The purified product was obtained in the tube with a temperature gradient.

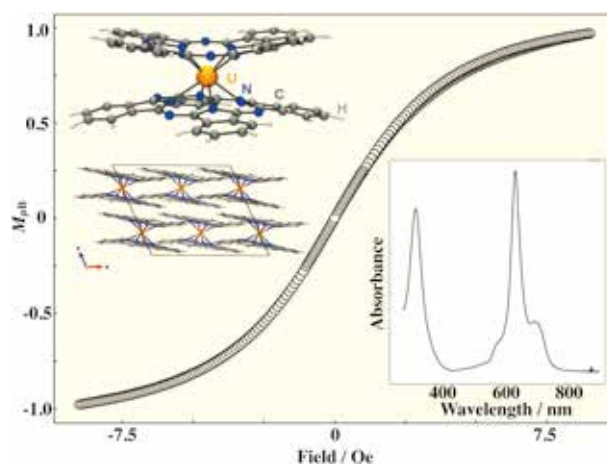


Fig. 1 Magnetization curve of bisphthalocyaninato-uranium(IV) indicated in Bohr magneton units. The sweeping external magnetic field:  $0 \rightarrow 90 \text{ k} \rightarrow -90 \text{ k} \rightarrow 90 \text{ k} \rightarrow 0 \text{ Oe}$ . The magnitude of magnetization approaches  $1 \mu\text{B}$ . A small hysteresis was observed in the positive magnetic field area. However, a slow magnetic relaxation phenomenon was not observed by AC magnetic measurement. Inset left: The molecule structure of UPc2 and its stack in the crystal. Inset right: The UV-Vis spectrum of UPc2. UPc2 has Q-band in the range of 580–700 nm, which is attributed to the  $\pi \rightarrow \pi^*$  transition of phthalocyaninato-rings.

The magnetic susceptibility of the lanthanide and uranium complexes in the constant and alternating magnetic field were measured using the PPMS [3]. In the case of the uranium complex, no SMM behavior was observed. It is conjectured that the energy separation between the lowest and second lowest substates is insufficient to exhibit the slow magnetic relaxation behaviors.

### References

- [1] N. Ishikawa et al. *J. Am. Chem. Soc.* **125**, 8694 (2003).
- [2] J. D. Rinehart et al. *J. Am. Chem. Soc.* **131**, 12558 (2009).
- [3] T. Fukuda et al. *Dalton Trans.* **46**, 12421 (2017).

Tomoo Yamamura (Corresponding author, Department of Nuclear Engineering, Kyoto University)

E-mail: yamamura@imr.tohoku.ac.jp

Ryuta Kasada (Head of Laboratory of Alpha-Ray Emitters)

URL: <http://alpha.imr.tohoku.ac.jp>

# Reliable and Precise Quantifications of Elemental Constituents in Steel Materials

## Analytical Research Core for Advanced Materials

Offers of elemental analyses are routinely accepted to provide the chemical composition in various metal and inorganic materials. Better accuracy, precision, and sensitivity of our analyses would be conducted on the basis of analytical improvements. Our recent studies on such an improvement are demonstrated.

The Analytical Research Core for Advanced Materials (ARCAM) uses various instrumental analyses, such as inductively coupled plasma atomic emission spectrometry, atomic absorption spectrometry (AAS), and gaseous CS/ON/H analyses. This report describes two analytical improvements in analysis of metallic materials that we suggested in 2017.

The oxygen content in a steel sample was accurately evaluated using a simple pre-treatment in inert gas fusion–infrared absorption spectrometry [1]. An over-estimated analytical value might be obtained in the oxygen quantification of steel samples because of surface-absorbed and surface-reacted oxygen. Several pieces of the specimen with different masses were prepared (e.g., column-shaped specimens of steel reference material (RM; JSS GS-2c) with masses 0.1, 0.2, 0.25, 0.5, and 1 g). The oxygen content values of these specimens were proportional to the surface area (Fig. 1). Therefore, a surface-oxygen-free analytical value of the oxygen content in the steel RM could be estimated by extrapolating this relation to be approximately  $13.5 \mu\text{g g}^{-1}$ .

A sequential internal standard method in flame, AAS was investigated for quantifying the alloyed nickel in a steel sample [2]. The nickel/iron absorbance ratio was used for the improvement of analytical precision. Relationships between the absorbance and iron concentration and the ranges of their linear calibration were tested for 23 iron atomic lines as the internal standard line. The results indicated that an allowable range of the concentration could be predicted from the product of the relative number density and the transition probability of the absorption lines (Fig. 2).

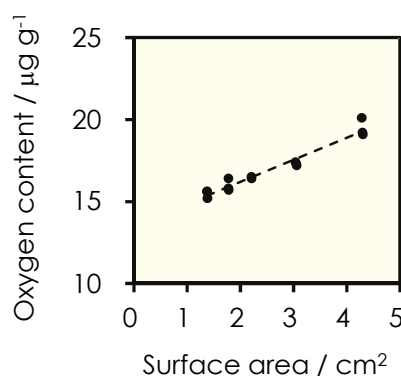


Fig. 1 Relationship between the analytical value of oxygen and the surface area in JSS GS-2c sample.

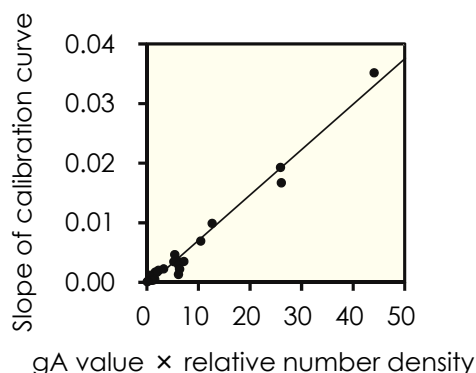


Fig. 2 Relationship between the slope of the calibration curve and the sensitivity factor (gA value × relative number density).

### References

- [1] T. Chiba, K. Wagatsuma, K. Takada, and K. Abiko, *Tetsu-to-Hagane*, **104**, 61 (2018).
- [2] T. Itagaki, T. Ashino, and K. Wagatsuma, *Bunseki Kagaku* **66**, 515 (2017).

Kenichi Nakayama (Corresponding Author, Analytical Research Core for Advanced Materials)

E-mail: ken1naka@imr.tohoku.ac.jp

Kazuaki Wagatsuma (Head of Analytical Research Core for Advanced Materials)

E-mail: wagatsuma@imr.tohoku.ac.jp

URL: <http://bunseki-core.imr.tohoku.ac.jp/>

## Author Index

Name	page	Name	page
<b>A</b>			
Akiyama, Eiji	11		
Amiya, Kenji	46		
Aoki, Dai	37		
<b>B</b>			
Bauer, Ernst-Wilhem Gerrit	49		
<b>C</b>			
Chiba, Akihiko	13		
<b>F</b>			
Fujita, Masaki	33, 50		
Fujiwara, Kozo	8, 48		
Furuhara, Tadashi	44		
<b>G</b>			
Goto, Takashi	25		
<b>H</b>			
Haga, Yoshinori	43		
Harada, Takayuki	31		
Hashimoto, Kenichiro	32		
Hashimoto, Yusuke	30		
<b>I</b>			
Ichitsubo, Tetsu	21		
Inoue, Koji	19		
<b>K</b>			
Kanazawa, Naoya	45		
Kasada, Ryuta	52		
Kato, Hidemi	22		
Kläui, Mathias	49		
Kubo, Momoji	10, 47		
<b>L</b>			
León, Alejandro	28		
<b>M</b>			
Masahashi, Naoya	46		
Matsuoka, Takashi	20		
Miyasaka, Hitoshi	34		
		Mohri, Tetsuo	39
<b>N</b>			
		Nagai, Yasuyoshi	19, 42, 43
		Nagumo, Kazuaki	19
		Nakayama, Kenichi	53
		Nojima, Tsutomu	51
		Nojiri, Hiroyuki	29, 45
		Nozawa, Jun	36
<b>O</b>			
		Ohno, Yutaka	18
		Ono, Kanta	47
		Orimo, Shin-ichi	23, 48
<b>S</b>			
		Saitoh, Eiji	30
		Sasaki, Takahiko	51
		Semboshi, Satoshi	44
		Shimizu, Yasuo	19
		Shiraishi, Takahisa	38
		Simura, Rayko	12
		Sugiyama, Kazumasa	12
<b>T</b>			
		Takagi, Shigeyuki	23
		Takahashi, Masae	47
		Takanashi, Koki	35
		Taniguchi, Kouji	34
		Tsukahara, Hiroshi	47
<b>W</b>			
		Wagatsuma, Kazuaki	14, 53
		Wei, Daixiu	15
<b>Y</b>			
		Yamamura, Tomoo	52
		Yamanaka, Kenta	13
		Yamazaki, Kaoru	39
		Yoshida, Kenta	42
		Yoshikawa, Akira	24
<b>Z</b>			
		Zhang, Yongjie	9

## Keyword Index

Keyword	page	Keyword	page
<b>A</b>		molecular dynamics	10
alloy	13, 24	multi-ferroics	29
atomic emission spectrometry	14	<b>N</b>	
<b>B</b>		nanostructure	15
bulk metallic glass	22	neutron diffraction	29
<b>C</b>		nuclear materials	19
chemical vapor deposition (CVD)	25	nucleation & growth	36
colloid	36	<b>O</b>	
corrosion	11, 15	optical properties	20
crystal growth	8, 24, 36	organic	32, 39
crystal structure	12, 21, 23	oxide	21, 31
<b>D</b>		<b>P</b>	
defects	13, 18, 20	phase transformation	9
deformation	22	photocatalytic	25
devices	31	piezoelectric	38
<b>E</b>		plasma diagnostic	14
electron doping	34	positron annihilation	19
electronic structure	33, 39	<b>Q</b>	
energy storage	21	quasicrystal	12
<b>F</b>		<b>R</b>	
first-principles calculations	23, 39	rare earths	28
fracture	10	<b>S</b>	
<b>G</b>		simulation	10
glow discharge plasma	14	solar cells	18
glass	32	spectroscopy	30
<b>H</b>		spin dynamics	35
heavy fermion	37	spin wave	30
high-magnetic field	29	spintronics	28
high strength steel	11	steel	9
hydride	23	strength	13
hydrogen evolution	25	superconducting	33, 37
hydrothermal	38	surface reaction	11, 15
<b>I</b>		<b>T</b>	
interface	8, 9, 18	thin films	31, 38
<b>M</b>		3D structure	20
magnetic properties	34, 35	<b>V</b>	
magnetism	30	vacancy	19
mechanical properties	22	voltage	28
metal	24	<b>X</b>	
metal-insulator transition	32	X-ray diffraction (XRD)	12
molecular beam epitaxy (MBE)	35	X-ray scattering	33
molecular devices	34		

### **Editors**

---

Kozo Fujiwara, Ryuta Kasada,  
Yoshinori Onose, Shigeyuki Takagi,  
Takeshi Seki, and Norihiko Okamoto

### **Editorial Staff**

---

Misa Y. Tomimatsu, Aki Oikawa, and Maki Sugawara

### **Printing**

---

HOKUTO Corporation

### **Organization**

---

Institute for Materials Research  
Tohoku University  
2-1-1 Katahira, Aoba-ku, Sendai 980-8577, Japan  
Tel. +81-(0)22-215-2144 Fax. +81-(0)22-215-2482

URL: <http://www.imr.tohoku.ac.jp/>  
E-mail: [pro-adm@imr.tohoku.ac.jp](mailto:pro-adm@imr.tohoku.ac.jp)